Fast Indirect Model Predictive Control for Variable Speed Drives

Wei Tian, *Member, IEEE,* Qifan Yang, *Member, IEEE,* Xiaonan Gao, *Member, IEEE,*
Petros Karamanakos, *Senior Member, IEEE,* Xingqi Yin, Ralph Kennel, *Life Senior Member, IEEE,*
and Marcelo Lobo Heldwein, *Senior Member, IEEE*

Abstract—This paper focuses on indirect model predictive control (MPC) for variable speed drives, such as induction and synchronous machine drives. The optimization problem underlying indirect MPC is typically written as a standard constrained quadratic programming (QP) problem, which requires a QP solver to find the optimal solution. Although many mature QP solvers exist, solving the QP problems in industrial real-time embedded systems in a matter of a few tens of microseconds remains challenging. Instead of using the complex general-purpose QP solvers, this paper proposes a geometrical method for isotropic machine drives and an analytical method for anisotropic machine drives to find the optimal output voltage. This is done by examining and subsequently exploiting the geometry of the associated optimization problems. Both methods are simple, and easy to implement on industrial control platforms. The effectiveness of the proposed geometrical and analytical methods is demonstrated by experimental results for an induction machine drive and an interior permanent-magnet synchronous machine drive, respectively.

Index Terms—Model predictive control (MPC), quadratic programming (QP), induction machine (IM), interior permanent-magnet synchronous machine (IPMSM).

I. INTRODUCTION

MODEL predictive control (MPC) has rapidly emerged in power electronics over the past decade due to the increase of the computational power available in real-time control platforms [1]–[4]. Thanks to its capability of dealing with system constraints, MPC is a promising alternative to the standard control methods, i.e., field-oriented control (FOC) and direct torque control (DTC), for drive systems [5]–[8].

A. State of the Art

Generally, MPC for drive systems can be classified into two main categories, i.e., *direct* MPC and *indirect* MPC, depending on whether there is a modulator or not. Direct MPC

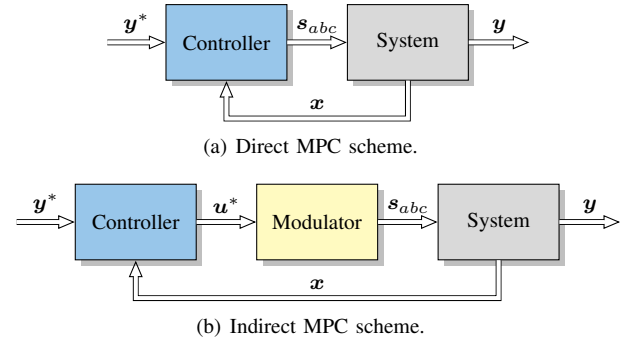(a) Direct MPC scheme.

(b) Indirect MPC scheme.

Figure 1. Direct and indirect MPC structures.

directly applies the switching signals to the power converter without requiring an intermediate modulation stage [9], see Fig. 1(a). By doing so, direct MPC obtains an excellent transient performance [1], [2]. Direct MPC can be split into three groups, i.e., MPC with hysteresis bounds [10], MPC with implicit modulator [11]–[13], and MPC with reference tracking, see Fig. 2. Direct MPC with reference tracking, also referred to as *finite-control-set* MPC (FCS-MPC), is the method most favored in academia due to its well-reported advantages such as its intuitive design procedure and straightforward implementation. FCS-MPC can be further divided into three subgroups according to the methods for solving the optimization problems, i.e., enumeration-based MPC [2], [6], [14], heuristic-preselection-based MPC [5], [7] and branch-and-bound-based MPC [15]–[19]. The most common used solution for direct MPC with short horizons is the so-called exhaustive enumeration method. With this method all the admissible switching states are enumerated, and the cost function is evaluated for each switching state. The switching state with the lowest cost is directly applied to the converter. Due to its straightforward implementation, the enumeration-based MPC has become the most popular MPC method for power electronics in the last decade [20], [21]. However, exhaustive enumeration quickly becomes computationally intractable when the prediction horizon increases. Hence, for long-horizon direct MPC, more sophisticated optimization methods are proposed. One is the so-called heuristic preselection strategy which is based on the assumption that the discrete-valued solution is normally close to the real-valued solution, i.e., the unconstrained solution of the direct MPC problem [5], [7]. Because of this, only a limited number of candidate integer solutions (i.e., switch positions) is evaluated in the optimization
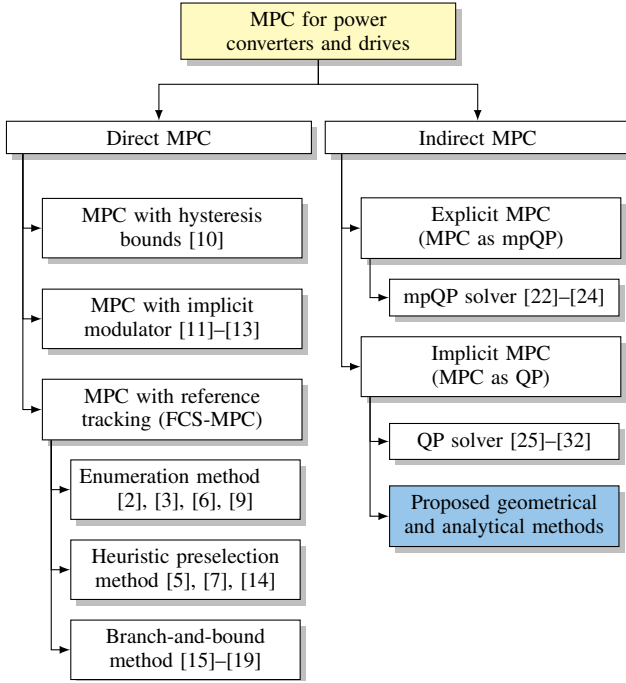
Figure 2. State-of-the-art MPC methods in power electronics.

procedure. Another more efficient approach relies on branch-and-bound techniques. In [15], the authors proposed the sphere decoding algorithm (SDA) as an effective branch-and-bound technique to reduce the computational burden for multistep direct MPC. Recently, to further mitigate the computational cost of direct MPC under transient conditions, some modified SDAs are proposed in [17]–[19].

However, the absence of the modulation stage in direct MPC leads to increased harmonic distortions and spread harmonic spectra due to the variable switching frequency. Such increased distortions can lead to increased iron and copper losses in the machine. Although some fixed switching frequency direct MPCs have been proposed to improve the steady-state performance [12], [22], the modulator-based *indirect* MPC, see Fig. 1(b), has been gaining more attention, due to its deterministic harmonic spectra and fixed switching frequency (i.e., deterministic power losses) [23]–[26]. The indirect MPC can be split into two groups, namely *explicit* MPC and *implicit* MPC, according to the different approaches for solving the optimization problem. Explicit MPC solves the optimization problem offline for all possible states with multiparametric quadratic programming (mpQP) solvers. Because of this, it was among the first MPC methods developed for power electronics due to the low online computational requirements [27]–[29]. However, it requires significant memory resources to store the offline-computed control law and this limits its applicability to optimization problems of very small size.

Owing to the recent development of open-source and commercial QP solvers for real-time embedded systems and the increase of the computational power, the *implicit* MPC has been gaining popularity in the electrical drive community in the last five years [26], [30]–[33]. The optimization problem of indirect MPC under consideration of system constraints is typically formulated as a constrained QP problem [34] and it is solved *online* by some iterative solver based on approaches such as active set, interior point and gradient projection methods [35]. Based on these approaches, more and more commercial off-the-shelf QP solvers for embedded systems come out in the last decades, e.g., `quadprog` (active set and interior point methods), `qpOASES` (active set method) and `FiOrdOs`(gradient method); a comprehensive assessment of these solvers is given in [36]. Among these, `qpOASES` is the most popular QP solver in the power electronics and drives community, see, e.g., [30], [37]–[39]. However, these off-the-shelf QP solvers are based on general-purpose algorithms and not tailored for power electronics applications, which require real-time solutions in the range of few tens of microseconds, and thus they cannot get the solution in a very efficient way for power electronics applications. Furthermore, the off-the-shelf QP solvers have specific requirements about the embedded software and hardware, hence they only can be implemented on a limited range of control platforms.

To address the aforementioned drawbacks, some custom-made QP solvers are proposed for electrical drive systems. In [31], [40], the tailored active set method is employed for online solving the constrained QP problem in permanent-magnet synchronous machine (PMSM) drives. In [12], [13], an efficient QP solver based on gradient projection method is implemented for an induction machine and a six-phase PMSM drive systems. However, in the implementation of these self-designed solvers, practitioners have to deal with the complete mathematical background of numerical optimization in detail. This hinders the wide spread of indirect MPC in electrical drives community.

B. Contribution

Hence, different from the numerical-method-based QP solvers, this paper provides an alternative way to solve the optimization problem in the electrical drives with problem-specific methods, i.e., geometrical and analytical methods, in a simple and efficient way. These methods are proposed based on the analysis of the constraints and geometry of the optimization problem. In three-phase voltage source inverter-fed drive systems, the constraint of the inverter output voltage is always hexagonal in an orthogonal $(\alpha\beta)$ frame, which can simplify the approach to determine the optimal solution. In recent research works [41], [42], algorithms are proposed to reduce computational burden by considering the hexagonal voltage constraints and the number of violated constraints. However, these methods do not make most the geometry of the optimization problem to further simplify the design approach. For isotropic and anisotropic machine drive systems, the contour lines of the MPC problem are in deterministic shapes. In particular, the contour lines of the MPC problem for isotropic machine drives, e.g., induction machine (IM), have circular shape. Then the optimization problem can be simplified to a problem of determining the shortest distance between a point and a line segment. With this observation, this paper proposes a simple geometrical method to obtain the optimal solution for isotropic machines.
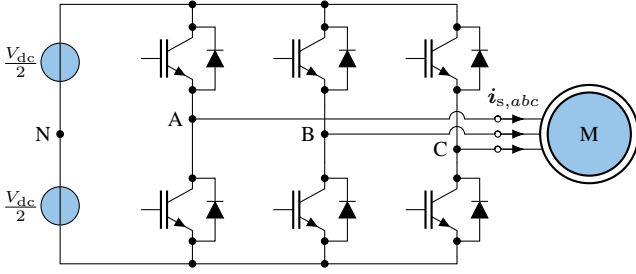
Figure 3. Two-level three-phase voltage source inverter driving the machine.

In anisotropic machine drive systems, e.g., interior permanent-magnet synchronous machine (IPMSM), the contour lines are elliptical and the geometrical method does not guarantee the optimal solution. In this case, an analytical method is proposed to calculate the optimal point on the fixed constraint line segment. These two purposed-built methods are both simple and easy to implement on any control platforms. In the remainder of this paper, the IM and IPMSM drives will be used as the examples of isotropic and anisotropic machine for the modelling and demonstrating the proposed methods.

The main contributions of this paper are summarized in the following.

1) A complete mathematical analysis of the geometry of the indirect MPC problems for IM and IPMSM drive systems is given based of the system parameters.
2) A geometrical method for induction IM drives and an analytical method for IPMSM drives is proposed to find the optimal applied voltage.
3) A comprehensive performance assessment is provided based on experimental results. The presented results show that the two proposed methods achieve exactly the same control performance as QP solvers but with less computational cost.

C. Paper Structure

This paper is structured as follows. Section II summarizes the mathematical models of the IM and IPMSM drives. Section III introduces the MPC scheme for electrical drives and the voltage constraints of the two-level inverter. A complete mathematical analysis of the geometry of the MPC problems for IM and IPMSM drives is detailed in Section IV. The proposed geometrical method for IM drives and analytical method for IPMSM drives is described in Sections V and VI, respectively. The experimental results are presented in Section VII, and conclusions are drawn in Section VIII.

II. MATHEMATICAL MODEL OF THE SYSTEM

Induction machines (isotropic machines) and IPMSMs (anisotropic machines) are the most common options in variable speed drive systems. In this section, a generic model for IM and IPMSM drive systems in the dq frame and the formulation of the control problem are presented.

The examined system consists of a three-phase two-level voltage source inverter and a motor, as shown in Fig. 3. The dc-link voltage is assumed to be constant and equal to its nominal value V_{dc}. The modeling of the system as well as the formulation of the control problem are done in the dq rotating reference frame. Therefore, the Park transformation matrix

$$T_p = \begin{bmatrix} \cos\theta & \sin\theta \\ -\sin\theta & \cos\theta \end{bmatrix} \tag{1}$$

is employed to map a variable $x_{\alpha\beta} = [x_\alpha \ x_\beta]^\top$ in the $\alpha\beta$ frame into a variable $x_{dq} = [x_d \ x_q]^\top$ in the dq frame, i.e., $x_{dq} = T_p x_{\alpha\beta}$. θ is the angle between the α-axis of the $\alpha\beta$ frame and the d-axis of the dq frame.

A. Induction Machine (isotropic machine)

The dynamics of the squirrel-cage IM can be fully described by the differential equations that involve the stator current $i_s = [i_d \ i_q]^\top$ and the rotor flux $\psi_r = [\psi_{rd} \ \psi_{rq}]^\top$.[1] Consider the dq reference frame rotating with the stator angular frequency ω_s. This leads to [16], [43]

$$\begin{bmatrix} \frac{di_s}{dt} \\ \frac{d\psi_r}{dt} \end{bmatrix} = \underbrace{\begin{bmatrix} -\frac{I_2}{\tau_s} - \omega_s J & (\frac{I_2}{\tau_r} - \omega_r J)\frac{L_m}{D} \\ \frac{L_m I_2}{\tau_r} & (\omega_r - \omega_s)J - \frac{I_2}{\tau_r} \end{bmatrix}}_{E_{IM}} \begin{bmatrix} i_s \\ \psi_r \end{bmatrix} + \underbrace{\begin{bmatrix} \frac{I_2 L_r}{D} \\ 0_2 \end{bmatrix}}_{F_{IM}} u_s \tag{2}$$

with

$$I_2 = \begin{bmatrix} 1 & 0 \\ 0 & 1 \end{bmatrix}, \ J = \begin{bmatrix} 0 & -1 \\ 1 & 0 \end{bmatrix}, \ 0_2 = \begin{bmatrix} 0 & 0 \\ 0 & 0 \end{bmatrix}, \ u_s = \begin{bmatrix} u_d \\ u_q \end{bmatrix},$$

where ω_r is the electrical angular speed of the rotor, R_s (R_r) is the stator (rotor) resistance, L_{ls} (L_{lr}) is the stator (rotor) leakage inductance, L_m is the mutual inductance, and u_s is the stator voltage in the dq frame, which is equal to the output voltage of the inverter. Moreover, $\tau_s = L_r D/(R_s L_r^2 + R_r L_m^2)$ and $\tau_r = L_r/R_r$ are the transient stator and rotor time constants, respectively, where the constant D is defined as $D = L_s L_r - L_m^2$, with the stator self-inductance $L_s = L_{ls} + L_m$ and the rotor self-inductance $L_r = L_{lr} + L_m$.

B. IPMSM (anisotropic machine)

The dynamic model of the IPMSM can be described by

$$\frac{di_s}{dt} = \underbrace{\begin{bmatrix} -\frac{R_s}{L_d} & \omega_r \frac{L_q}{L_d} \\ -\omega_r \frac{L_d}{L_q} & -\frac{R_s}{L_q} \end{bmatrix}}_{E_{IPMSM}} i_s + \underbrace{\begin{bmatrix} \frac{1}{L_d} & 0 \\ 0 & \frac{1}{L_q} \end{bmatrix}}_{F_{IPMSM}} u_s + \underbrace{\begin{bmatrix} 0 \\ -\omega_r \frac{\psi_f}{L_q} \end{bmatrix}}_{w(t)}, \tag{3}$$

where L_d and L_q are the stator inductance on d- and q-axis, respectively, and ψ_f is the permanent magnet flux linkage.

C. Generic State-space Representation

Choosing the stator voltage u_s as the input vector u, i.e., $u = u_s = [u_d \ u_q]^\top$ and the stator current i_s as the output vector y, i.e., $y = i_s = [i_d \ i_q]^\top$, both models described

---

[1]To simplify the notation, the subscript dq for vectors in the dq frame is omitted
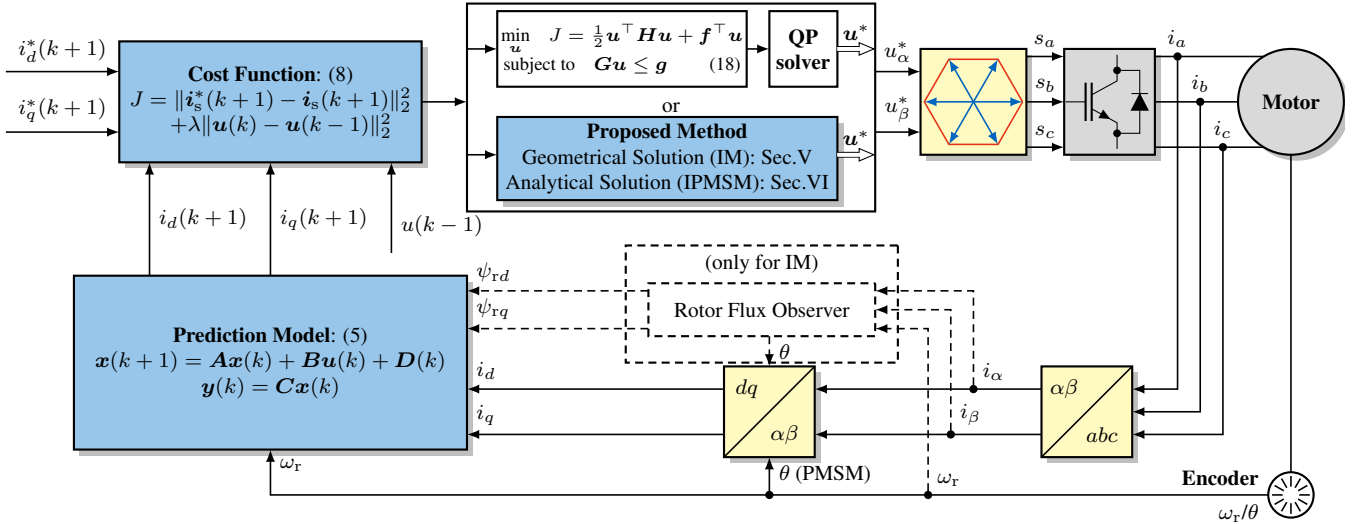
Figure 4. Block diagram of the indirect MPC scheme for electrical drives.

in (2) and (3) can be written with the generic state-space representation

$$\frac{d\boldsymbol{x}(t)}{dt} = \boldsymbol{E}\boldsymbol{x}(t) + \boldsymbol{F}\boldsymbol{u}(t) + \boldsymbol{w}(t) \tag{4a}$$

$$\boldsymbol{y}(t) = \boldsymbol{C}\boldsymbol{x}(t), \tag{4b}$$

where the state vector is $\boldsymbol{x} = [i_d\ i_q\ \psi_{\mathrm{rd}}\ \psi_{\mathrm{rq}}]^\top$ for IM, or $\boldsymbol{x} = [i_d\ i_q]^\top$ for IPMSM and $\boldsymbol{w}(t)$ is $\boldsymbol{0}$ for IM. The output matrices $\boldsymbol{C}$ for IM and IPMSM are

$$\boldsymbol{C}_{\mathrm{IM}} = \begin{bmatrix} 1 & 0 & 0 & 0 \\ 0 & 1 & 0 & 0 \end{bmatrix} \text{ and } \boldsymbol{C}_{\mathrm{IPMSM}} = \begin{bmatrix} 1 & 0 \\ 0 & 1 \end{bmatrix}, \text{respectively.}$$

By using the forward Euler approximation, the discrete-time state-space model of the system is of the form

$$\boldsymbol{x}(k+1) = \boldsymbol{A}\boldsymbol{x}(k) + \boldsymbol{B}\boldsymbol{u}(k) + \boldsymbol{d}(k) \tag{5a}$$

$$\boldsymbol{y}(k) = \boldsymbol{C}\boldsymbol{x}(k), \tag{5b}$$

with $k \in \mathbb{N}$, $\boldsymbol{A} = \boldsymbol{I} + \boldsymbol{E}T_{\mathrm{s}}$, $\boldsymbol{B} = \boldsymbol{F}T_{\mathrm{s}}$ and $\boldsymbol{d}(k) = \boldsymbol{w}(k)T_{\mathrm{s}}$, where the dimension of the identity matrix $\boldsymbol{I}$ is 4 for IM and is 2 for IPMSM, and T_{s} is the sampling interval.

To simplify the illustration of the voltage constraints, it is better to use the $\alpha\beta$-plane voltage as the input vector in (5), rather than the dq-plane voltage. Hence, in the following parts of this paper, we have $\boldsymbol{u} = \boldsymbol{u}_{\mathrm{s},\alpha\beta} = [u_\alpha\ u_\beta]^\top$. In this case, the input matrix is transformed as $\boldsymbol{B} = \boldsymbol{F}\boldsymbol{T}_{\mathrm{p}}T_{\mathrm{s}}$, where $\boldsymbol{T}_{\mathrm{p}}$ is the Park transformation matrix shown in (1).

III. MODEL PREDICTIVE CURRENT CONTROL OF IM AND IPMSM DRIVE

The control problem of MPC with reference tracking over a finite prediction horizon can be addressed through the minimization of the general cost function [34]

$$J = \sum_{j=0}^{N_p-1} \|\boldsymbol{y}^*(k+1+j) - \boldsymbol{y}(k+1+j)\|_2^2 + \sum_{i=0}^{N_u-1} \lambda\|\Delta\boldsymbol{u}(k+i)\|_2^2, \tag{6}$$

where $\|\cdot\|_2^2$ is the square of 2-norm, $\boldsymbol{y}^*$ and $\boldsymbol{y}$ are the reference and predicted value of the output, N_p and N_u are the prediction and control horizon, λ is the weighting factor with $\lambda \geq 0$, and $\Delta\boldsymbol{u}$ is the input increment which can be denoted as

$$\Delta\boldsymbol{u}(k) = \boldsymbol{u}(k) - \boldsymbol{u}(k-1). \tag{7}$$

In this paper, we only consider the most commonly used one-step predictive control, i.e., $N_p = 1$ and $N_u = 1$. With (5b) and (7), cost function (6) can be simplified as

$$J = \|\boldsymbol{i}_{\mathrm{s}}^*(k+1) - \boldsymbol{i}_{\mathrm{s}}(k+1)\|_2^2 + \lambda\|\boldsymbol{u}(k) - \boldsymbol{u}(k-1)\|_2^2. \tag{8}$$

The first term in (8) penalizes the predicted stator current error at the next time step $k+1$ and the second term penalizes the control effort at time step k.

A. Quadratic Programming (QP) Problem Formulation

With the state-space model expressed in (5), the cost function (8) can be written as

$$\begin{aligned} J =& \|\underbrace{\boldsymbol{CB}}_{\boldsymbol{M}}\boldsymbol{u}(k) + \underbrace{\boldsymbol{CAx}(k) + \boldsymbol{Cd}(k) - \boldsymbol{i}_s^*(k+1)}_{\boldsymbol{r}}\|_2^2 \\ &+ \lambda\|\boldsymbol{u}(k) - \boldsymbol{u}(k-1)\|_2^2 \\ =& \|\boldsymbol{M}\boldsymbol{u}(k) + \boldsymbol{r}\|_2^2 + \lambda\|\boldsymbol{u}(k) - \boldsymbol{u}(k-1)\|_2^2. \end{aligned} \tag{9}$$

At time step k, $\boldsymbol{x}(k)$, $\boldsymbol{d}(k)$, $\boldsymbol{u}(k-1)$ and $\boldsymbol{i}_{\mathrm{s}}^*(k+1)$ are known and $\boldsymbol{r}$ can be regarded as a constant. Therefore, the only unknown variable of the cost function at time step k is $\boldsymbol{u}(k)$.

By expanding the square of the 2-norm in (9), the cost function J can be expressed as

$$
\begin{aligned}
J =& \frac{1}{2}\boldsymbol{u}(k)^\top \underbrace{(2\boldsymbol{M}^\top \boldsymbol{M} + 2\lambda \boldsymbol{I})}_{\boldsymbol{H}}\boldsymbol{u}(k) \\
&+ \underbrace{(2\boldsymbol{M}^\top \boldsymbol{r} - 2\lambda \boldsymbol{u}(k-1))^\top}_{\boldsymbol{f}}\boldsymbol{u}(k) \\
&+ \underbrace{\boldsymbol{r}^\top \boldsymbol{r} + \lambda \boldsymbol{u}^\top(k-1)\boldsymbol{u}(k-1)}_{c \;(\text{constant})} \\
=& \frac{1}{2}\boldsymbol{u}^\top(k)\boldsymbol{H}\boldsymbol{u}(k) + \boldsymbol{f}^\top \boldsymbol{u}(k) + c.
\end{aligned}
\tag{10}
$$

Dropping the constant c, the optimization problem results in the unconstrained QP problem[2]

$$
\underset{\boldsymbol{u}}{\text{minimize}} \quad J = \frac{1}{2}\boldsymbol{u}^\top \boldsymbol{H}\boldsymbol{u} + \boldsymbol{f}^\top \boldsymbol{u},
\tag{11}
$$

where $\boldsymbol{H}$ is the Hessian matrix. In our case $\boldsymbol{H}$ is positive definite, meaning that (11) is a convex QP. In the absence of the constraints, the convex QP problem can be solved by setting the gradient of (11) equal to zero

$$
\nabla J = \boldsymbol{0}.
\tag{12}
$$

Then the unconstrained solution is computed as[3]

$$
\boldsymbol{u}^*_{\text{unc}} = -\boldsymbol{H}^{-1}\boldsymbol{f}.
\tag{13}
$$

B. Voltage Constraints

1) Incircle: For three-phase two-level inverters, the feasible output voltage region is represented by a hexagonal convex region in the $\alpha\beta$ stationary frame as shown in Fig. 5. However, in many practical applications, the output is limited to the incircle of the hexagon (also called linear modulation region) to simplify the design of control algorithms, because the mathematical representation of the hexagonal constraint is more complex [32], [44], [45]. The incircle constraint can be presented as

$$
u_\alpha^2 + u_\beta^2 \le R^2,
\tag{14}
$$

where $R = \frac{V_{\text{dc}}}{\sqrt{3}}$ is the radius of the incircle.

In transients, the unconstrained solution (13) may often exceed the incircle voltage limit. To deal with this in practice, the commanded voltage is often limited to the incircle by means of scaling. More specifically, when $\boldsymbol{u}^*_{\text{unc}}$ is out of the incircle, the saturated voltage $\boldsymbol{u}^*_{\text{sat}}$ is obtained by scaling $\boldsymbol{u}^*_{\text{unc}}$ to the incircle voltage limit with

$$
\boldsymbol{u}^*_{\text{sat}} = \frac{\boldsymbol{u}^*_{\text{unc}}}{\sqrt{u^{*2}_{\alpha,\text{unc}} + u^{*2}_{\beta,\text{unc}}}}R.
\tag{15}
$$

Otherwise, when the $\boldsymbol{u}^*_{\text{unc}}$ is in the incircle, then we have $\boldsymbol{u}^*_{\text{sat}} = \boldsymbol{u}^*_{\text{unc}}$.

In [32], the aforementioned incircle saturation with scaling is applied to simplify the optimization problem for the implicit MPC in a PMSM drive. Although this implicit unconstrained

---

[2]To simplify the notation, in the following part of this section the time indication from $\boldsymbol{u}(k)$ is omitted

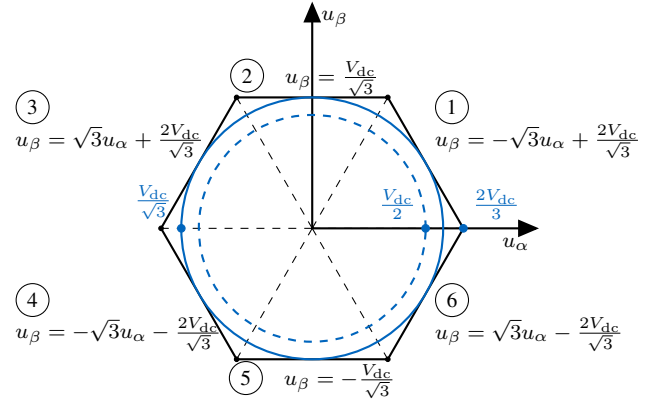[3]The superscript * represents the reference value for the modulator.

Figure 5. Voltage constraints of the voltage source inverter (VSI).

MPC with incircle saturation, referred to as *saturated* MPC in the remainder of this paper, has good performance in steady state, it results in a sluggish response in transients due to the underutilization of the dc-link voltage. On the contrary, the indirect MPC fully utilizes the dc-link voltage and achieves better dynamic behavior by considering the hexagon voltage constraints. Hence, in the following proposed methods, the hexagon is used as the constraints to improve the dynamic response.

2) Hexagon: The six border line segments of the hexagon can be expressed as six linear equations shown in Fig. 5. These equations, i.e., constraints, can be written in the compact form

$$
\underbrace{\begin{bmatrix} \sqrt{3} & 1 \\ 0 & 1 \\ -\sqrt{3} & 1 \\ -\sqrt{3} & -1 \\ 0 & -1 \\ \sqrt{3} & -1 \end{bmatrix}}_{\boldsymbol{G}} \underbrace{\begin{bmatrix} u_\alpha \\ u_\beta \end{bmatrix}}_{\boldsymbol{u}} \le \underbrace{\begin{bmatrix} \frac{2V_{\text{dc}}}{\sqrt{3}} \\ \frac{V_{\text{dc}}}{\sqrt{3}} \\ \frac{2V_{\text{dc}}}{\sqrt{3}} \\ \frac{2V_{\text{dc}}}{\sqrt{3}} \\ \frac{V_{\text{dc}}}{\sqrt{3}} \\ \frac{2V_{\text{dc}}}{\sqrt{3}} \end{bmatrix}}_{\boldsymbol{g}}.
\tag{16}
$$

In doing so, the standard inequality constraint can be expressed as

$$
\boldsymbol{G}\boldsymbol{u} \le \boldsymbol{g}.
\tag{17}
$$

With the above, the MPC optimization problem that accounts for the hexagon voltage constraints can be written as a standard constrained QP of the form

$$
\underset{\boldsymbol{u}}{\text{minimize}} \quad J = \frac{1}{2}\boldsymbol{u}^\top \boldsymbol{H}\boldsymbol{u} + \boldsymbol{f}^\top \boldsymbol{u}
\tag{18a}
$$
$$
\text{subject to} \quad \boldsymbol{G}\boldsymbol{u} \le \boldsymbol{g},
\tag{18b}
$$

Constrained convex QPs such as (18) are typically solved with approaches such as active set, interior point and gradient projection methods [35]. The complete block diagram of the implicit MPC scheme with QP solver for electrical drives is shown in Fig. 4.

Although these QP methods came out several decades ago in the numerical optimization field, solving the QP problems in industrial real-time embedded systems in a matter of a few

tens of microseconds remains challenging. For the design of QP solvers for drive systems, readers can refer to works like [12], [46] (gradient projection method) and [31], [40], [47] (active set method). Different from these works, this paper proposes simple and efficient methods to find the optimal solution for the constrained MPC of electrical drives, instead of using complex QP solvers.

IV. ANALYSIS

A. Unconstrained Solution inside the Hexagon

Firstly, let's consider the simplest case when the unconstrained solution (13) is inside the hexagon. In this case, the voltage constraints have no influence on the results. Hence, the optimal solution is the unconstrained solution

$$\boldsymbol{u}^*_{\text{opt}} = \boldsymbol{u}^*_{\text{unc}} = -\boldsymbol{H}^{-1}\boldsymbol{f}. \tag{19}$$

B. Unconstrained Solution outside the Hexagon

Another case is when the unconstrained solution is outside the hexagon. In this case, we have to take the contour of the cost function and the voltage constraints into consideration. Since the Hessian matrix $\boldsymbol{H}$ determines the shape of the contour for a quadratic function, with the help of (10) it can be written as

$$\boldsymbol{H} = 2\boldsymbol{M}^\top \boldsymbol{M} + 2\lambda \boldsymbol{I} = 2(\boldsymbol{CB})^\top (\boldsymbol{CB}) + 2\lambda \boldsymbol{I}, \tag{20}$$

where $\boldsymbol{C}$ and $\boldsymbol{B}$ depend only on the parameters of the drive.

1) Contour of Cost Function for IM: When the induction machine drive is considered, (20) becomes

$$\boldsymbol{H} = \left(\frac{2L_{\text{r}}^2 T_{\text{s}}^2}{D^2} + 2\lambda\right) \begin{bmatrix} 1 & 0 \\ 0 & 1 \end{bmatrix}. \tag{21}$$

In this case, $\boldsymbol{H}$ is a scalar matrix[4], and the contour lines of (18a) are circular, as shown in Fig. 6(a). The analysis of IM also can be extended to any isotropic machine, e.g., surface-mounted permanent magnet synchronous machine (SPMSM).

2) Contour of Cost Function for IPMSM: When IPMSM drives are of interest, the Hessian matrix $\boldsymbol{H}$ becomes

$$\boldsymbol{H} = 2T_{\text{s}}^2 \begin{bmatrix} \frac{\cos^2 \theta}{L_d^2} + \frac{\sin^2 \theta}{L_q^2} + \frac{\lambda}{T_{\text{s}}^2} & \frac{\sin \theta \cos \theta}{L_d^2} - \frac{\sin \theta \cos \theta}{L_q^2} \\ \frac{\sin \theta \cos \theta}{L_d^2} - \frac{\sin \theta \cos \theta}{L_q^2} & \frac{\sin^2 \theta}{L_d^2} + \frac{\cos^2 \theta}{L_q^2} + \frac{\lambda}{T_{\text{s}}^2} \end{bmatrix}. \tag{22}$$

Since $L_d \neq L_d$ in IPMSMs, the Hessian matrix $\boldsymbol{H}$ is symmetric but not a scalar. Hence, the contour lines of the associated optimization problem (18) are elliptical, see Fig. 6(b).

In the following, two different methods are proposed for IM and IPMSM drives depending on the type of the contour map.

[4]A scalar matrix is a type of square matrix in which its principal diagonal elements are all equal and off-diagonal elements are all zero. It is a multiplicative constant of an identity matrix.
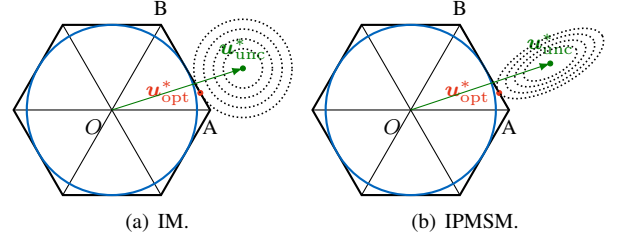

Figure 6. Contour line for IM and IPMSM

(a) IM.   (b) IPMSM.

V. PROPOSED GEOMETRICAL METHOD FOR IM DRIVES

As shown in Fig. 7, if the unconstrained solution, e.g., point G, is outside the hexagon, then the optimal solution $\boldsymbol{u}^*_{\text{opt}}$ will locate on the borderline AB. As discussed in Section IV, contour lines of the indirect MPC problem (18) for IM drives are circular. In this case, the value of the cost function only depends on the distance between unconstrained solution G and the constrained solution on the line segment AB. Hence, the problem of minimizing the cost function becomes a problem of determining the closest point on AB to G. Observing Fig. 7, it can be deduced that the optimal solution (point H) should be the closest point to G, i.e., the point on the line segment AB that leads to $AB \perp GH$. The remainder of this section focuses on the calculation of H in $\alpha\beta$ coordinate.

In Fig. 7, $\overrightarrow{OG}$ can be expressed as

$$\overrightarrow{OG} = \overrightarrow{OI} + \overrightarrow{IG},$$

where point I is on the extension line of the line segment $\overline{OA}$ with $IG \parallel OB$. With $\overrightarrow{OI} = d'_1 \cdot \overrightarrow{OA}$ and $\overrightarrow{IG} = d'_2 \cdot \overrightarrow{OB}$, we have

$$\overrightarrow{OG} = d'_1 \cdot \overrightarrow{OA} + d'_2 \cdot \overrightarrow{OB}, \tag{23}$$

where d'_1 and d'_2 are the coefficients that show the utilization of $\overrightarrow{OA}$ and $\overrightarrow{OB}$, respectively. As $\overrightarrow{OA}$ and $\overrightarrow{OB}$ are known, then (23) can be rewritten as

$$\boldsymbol{u}^*_{\text{unc}} = \underbrace{\begin{bmatrix} u^*_{\alpha,\text{unc}} \\ u^*_{\beta,\text{unc}} \end{bmatrix}}_{\overrightarrow{OG}} = d'_1 \underbrace{\begin{bmatrix} \frac{2V_{\text{dc}}}{3} \\ 0 \end{bmatrix}}_{\overrightarrow{OA}} + d'_2 \underbrace{\begin{bmatrix} \frac{V_{\text{dc}}}{3} \\ \frac{V_{\text{dc}}}{\sqrt{3}} \end{bmatrix}}_{\overrightarrow{OB}}. \tag{24}$$

With (24), the coefficients can be obtained as

$$d'_1 = \frac{3u^*_{\alpha,\text{unc}} - \sqrt{3}u^*_{\beta,\text{unc}}}{2V_{\text{dc}}}, \text{ and } d'_2 = \frac{\sqrt{3}u^*_{\beta,\text{unc}}}{V_{\text{dc}}}. \tag{25}$$

The coefficients in (25) are only for the situation when $\boldsymbol{u}^*_{\text{unc}}$ locates in Sector 1. For the general situation, the angle θ given by

$$\theta = \text{atan2}\left(u^*_{\beta,\text{unc}}, u^*_{\alpha,\text{unc}}\right), \quad \theta \in (-\pi, \pi] \tag{26}$$

can be used to determine the sector and then the value of d'_1 and d'_2 for a given sector can be obtained based on Table I.

Then, the optimal solution $\boldsymbol{u}^*_{\alpha\beta,\text{opt}}$ can also be described as

$$\boldsymbol{u}^*_{\alpha\beta,\text{opt}} = \overrightarrow{OH} = \overrightarrow{OJ} + \overrightarrow{JH},$$

where point J is on the line segment $\overline{OA}$ with $JH \parallel OB$. Similarly, with $\overrightarrow{OJ} = d_1 \cdot \overrightarrow{OA}$ and $\overrightarrow{JH} = d_2 \cdot \overrightarrow{OB}$, we have

$$\boldsymbol{u}^*_{\alpha\beta,\text{opt}} = d_1 \cdot \overrightarrow{OA} + d_2 \cdot \overrightarrow{OB}, \tag{27}$$
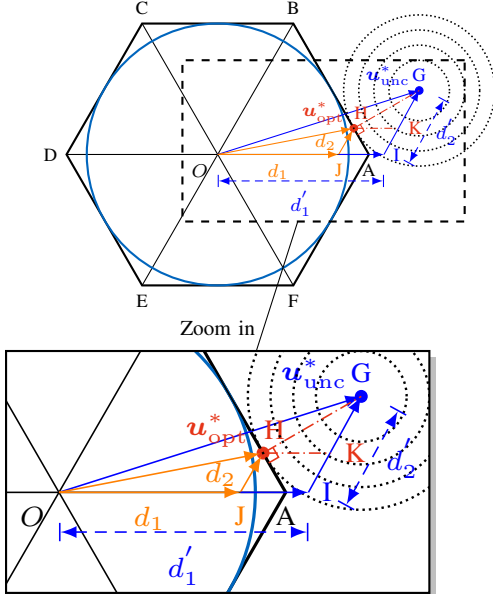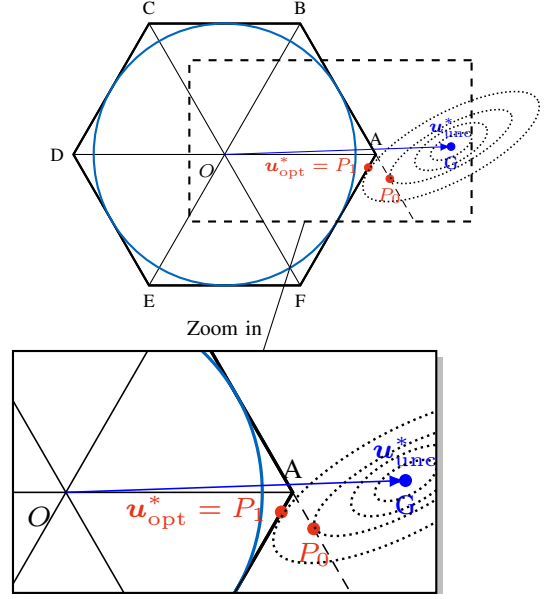
Figure 7. Proposed geometrical method for IM drive.

Figure 8. Proposed analytical method for IPMSM drive.

Substituting $\overrightarrow{HK}$ and $\overrightarrow{KG}$ with (29) and (30) yields

$$d_1' - d_1 = d_2' - d_2. \tag{33}$$

With (28) and (33), d_1 and d_2 can be easily found, i.e.,

$$d_1 = \frac{d_1' - d_2' + 1}{2}, \tag{34a}$$

$$d_2 = \frac{d_2' - d_1' + 1}{2}. \tag{34b}$$

Finally, with (27) and (34), the optimal reference voltage $\boldsymbol{u}_{\alpha\beta,\mathrm{opt}}^*$ is derived. This simple and direct procedure is also illustrated in Fig. 9.

Note that the proposed geometrical method is an intuitive approach. Although similar approaches have been used in for overmodulation and saturation in drive systems, e.g., [48], they merely compute the control action with traditional linear controllers, and then simply saturate it to the hexagon with different strategies, e.g., minimum voltage amplitude error and minimum voltage phase error methods, which cannot always guarantee the optimal solution for control objectives, e.g., stator current. Here the proposed MPC-based geometrical method formulates the control problem into a constrained QP problem and obtains the solution based on the analysis of the contour map of the cost function. In doing so, the characteristics of isotropic machines are considered, and control and saturation are done at the same time, i.e., in a coordinated manner, hence the optimal solution can be guaranteed.

VI. PROPOSED ANALYTICAL METHOD FOR IPMSM DRIVES

Since the contour maps of the MPC problem for IPMSM drives has elliptical form, the geometrical method proposed in the previous section is not applicable. To rectify this issue, an analytical method is proposed in this section to obtain the optimal solution $\boldsymbol{u}_{\mathrm{opt}}^*$ when the unconstrained solution $\boldsymbol{u}_{\mathrm{unc}}^*$ is out of the hexagon.

TABLE I
COEFFICIENTS

Sector	θ	d_1'	d_2'
1	$(0, \frac{\pi}{3}]$	$\frac{3u_{\alpha,\mathrm{unc}}^* - \sqrt{3}u_{\beta,\mathrm{unc}}^*}{2V_{\mathrm{dc}}}$	$\frac{\sqrt{3}u_{\beta,\mathrm{unc}}^*}{V_{\mathrm{dc}}}$
2	$(\frac{\pi}{3}, \frac{2\pi}{3}]$	$\frac{3u_{\alpha,\mathrm{unc}}^* + \sqrt{3}u_{\beta,\mathrm{unc}}^*}{2V_{\mathrm{dc}}}$	$\frac{-3u_{\alpha,\mathrm{unc}}^* + \sqrt{3}u_{\beta,\mathrm{unc}}^*}{2V_{\mathrm{dc}}}$
3	$(\frac{2\pi}{3}, \pi]$	$\frac{\sqrt{3}u_{\beta,\mathrm{unc}}^*}{V_{\mathrm{dc}}}$	$\frac{-3u_{\alpha,\mathrm{unc}}^* - \sqrt{3}u_{\beta,\mathrm{unc}}^*}{2V_{\mathrm{dc}}}$
4	$(-\pi, -\frac{2\pi}{3}]$	$\frac{-3u_{\alpha,\mathrm{unc}}^* + \sqrt{3}u_{\beta,\mathrm{unc}}^*}{2V_{\mathrm{dc}}}$	$-\frac{\sqrt{3}u_{\beta,\mathrm{unc}}^*}{V_{\mathrm{dc}}}$
5	$(-\frac{2\pi}{3}, -\frac{\pi}{3}]$	$-\frac{3u_{\alpha,\mathrm{unc}}^* + \sqrt{3}u_{\beta,\mathrm{unc}}^*}{2V_{\mathrm{dc}}}$	$\frac{3u_{\alpha,\mathrm{unc}}^* - \sqrt{3}u_{\beta,\mathrm{unc}}^*}{2V_{\mathrm{dc}}}$
6	$(-\frac{\pi}{3}, 0]$	$-\frac{\sqrt{3}u_{\beta,\mathrm{unc}}^*}{V_{\mathrm{dc}}}$	$\frac{3u_{\alpha,\mathrm{unc}}^* + \sqrt{3}u_{\beta,\mathrm{unc}}^*}{2V_{\mathrm{dc}}}$

where d_1 and d_2 are the coefficients that show the utilization of $\overrightarrow{OA}$ and $\overrightarrow{OB}$, respectively. Different from the unconstrained solution outside the hexagon, the optimal solution $\boldsymbol{u}_{\alpha\beta,\mathrm{opt}}^*$ on the borderline meets the following relationship

$$d_1 + d_2 = 1. \tag{28}$$

It can also be observed from Fig. 7 that

$$\overrightarrow{HK} = \overrightarrow{JI} = \overrightarrow{OI} - \overrightarrow{OJ},$$

where point K is on the line segment $\overline{IG}$ with $HK \parallel OA$. With $\overrightarrow{OI} = d_1' \cdot \overrightarrow{OA}$ and $\overrightarrow{OJ} = d_1 \cdot \overrightarrow{OA}$, it follows that

$$\overrightarrow{HK} = (d_1' - d_1) \cdot \overrightarrow{OA}. \tag{29}$$

Similarly, it can be shown that

$$\overrightarrow{KG} = (d_2' - d_2) \cdot \overrightarrow{OB} \tag{30}$$

Moreover, since it holds that

$$\angle GHK = \angle HGK = \frac{\pi}{6}, \tag{31}$$

it follows that

$$|\overrightarrow{HK}| = |\overrightarrow{KG}|. \tag{32}$$

Similar to the geometrical method, the sector for $\boldsymbol{u}^*_{\text{unc}}$ is determined with (26). Taking Fig. 6(b) as example, if $\boldsymbol{u}^*_{\text{unc}}$ locates in Sector 1, it is first assumed that the optimal constrained solution $\boldsymbol{u}^*_{\text{opt}}$ is on one borderline of the hexagon which is in the same sector as $\boldsymbol{u}^*_{\text{unc}}$ (here is borderline AB). Without loss of generality, this borderline can be expressed as

$$u_\beta = a u_\alpha + b, \tag{35}$$

where the coefficients a and b can be determined based on θ according to Table II.

Table II
BOUNDARY

Sector	θ	a	b
1	$(0, \frac{\pi}{3}]$	$-\sqrt{3}$	$\frac{2V_{\text{dc}}}{\sqrt{3}}$
2	$(\frac{\pi}{3}, \frac{2\pi}{3}]$	0	$\frac{V_{\text{dc}}}{\sqrt{3}}$
3	$(\frac{2\pi}{3}, \pi]$	$\sqrt{3}$	$\frac{2V_{\text{dc}}}{\sqrt{3}}$
4	$(-\pi, -\frac{2\pi}{3}]$	$-\sqrt{3}$	$\frac{-2V_{\text{dc}}}{\sqrt{3}}$
5	$(-\frac{2\pi}{3}, -\frac{\pi}{3}]$	0	$\frac{-V_{\text{dc}}}{\sqrt{3}}$
6	$(-\frac{\pi}{3}, 0]$	$\sqrt{3}$	$\frac{-2V_{\text{dc}}}{\sqrt{3}}$

Second, the cost function in (9) can be rewritten as

$$J = \left\| \underbrace{\begin{bmatrix} m_{11} & m_{12} \\ m_{21} & m_{22} \end{bmatrix}}_{\boldsymbol{M}} \begin{bmatrix} u_\alpha \\ u_\beta \end{bmatrix} + \underbrace{\begin{bmatrix} r_1 \\ r_2 \end{bmatrix}}_{\boldsymbol{r}} \right\|_2^2 + \lambda \left\| \underbrace{\begin{bmatrix} u_\alpha \\ u_\beta \end{bmatrix}}_{\boldsymbol{u}(k)} - \underbrace{\begin{bmatrix} u_{\alpha 0} \\ u_{\beta 0} \end{bmatrix}}_{\boldsymbol{u}(k-1)} \right\|_2^2 \tag{36}$$

Inserting (35) in (36) leads to a quadratic function of u_α

$$J = a_q u_\alpha^2 + b_q u_\alpha + c_q, \tag{37}$$

where a_q, b_q and c_q are coefficients which are given in Appendix A. It is obvious that $a_q > 0$, so (37) reaches the minimum at[5]

$$u_\alpha^0 = -\frac{b_q}{2a_q}. \tag{38}$$

With (35), u_β can be obtained as

$$u_\beta^0 = -\frac{a b_q}{2a_q} + b. \tag{39}$$

Accordingly, the angle of this solution is

$$\theta^0 = \text{atan2}\left(u_\beta^0, u_\alpha^0 \right). \tag{40}$$

Following, the constraints in (17) are simplified as

$$\theta \in (\theta_{\min}, \theta_{\max}], \tag{41}$$

where $\theta_{\min}$ and $\theta_{\max}$ are the angles of the two endpoints of the line segment $\overline{AB}$ as listed in Table II.

If θ^0 meets the constraint in (41), then $[u_\alpha^0 \ u_\beta^0]^\top$ locates on the line segment $\overline{AB}$, as illustrated in Fig. 6(b). This yields

$$\boldsymbol{u}^*_{\text{opt}} = \begin{bmatrix} u_\alpha^0 \\ u_\beta^0 \end{bmatrix}, \tag{42}$$

[5]The superscript 0 represents the initial guess point, and the superscript 1 represents the second guess point.
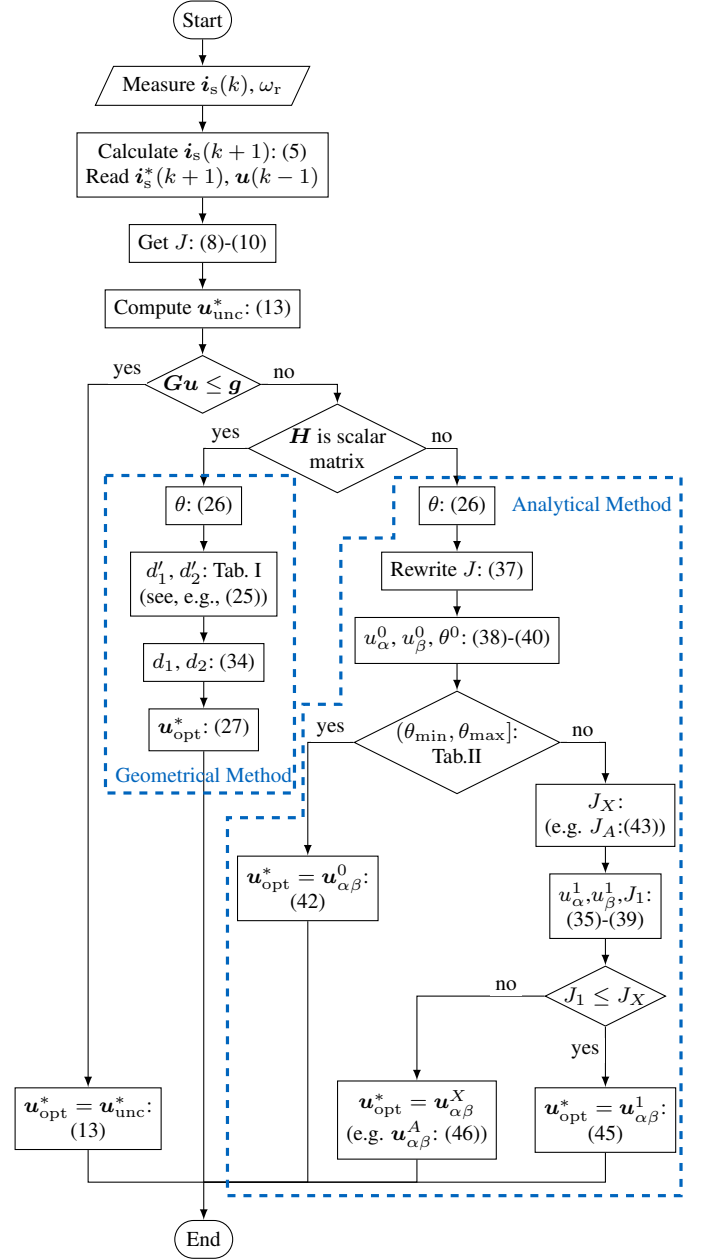

Figure 9. Flowchart of the proposed implicit MPC methods for IM and IPMSM drives.

Otherwise, θ^0 is in an adjacent sector and $[u_\alpha^0 \ u_\beta^0]^\top$ is on the extension of the line segment $\overline{AB}$, e.g., point P_0 in Fig. 8. In this case, P_0 in Sector 6 cannot be the solution in the pre-selected sector 1. For this reason, point A ($[u_\alpha^A \ u_\beta^A]^\top$) is considered as the sub-optimal solution. The value of the cost function for point A is

$$J_A = a_q u_\alpha^{A^2} + b_q u_\alpha^A + c_q. \tag{43}$$

Note that for this part of the procedure described in Fig. 9, J_X is used to denote the sub-optimal solution, where X stands for one of the six vertices of the hexagon, i.e., A, B, ..., F in Fig. 8.

As point A is considered as the sub-optimal solution, the line segment $\overline{AF}$ is considered as the new linear constraint. In
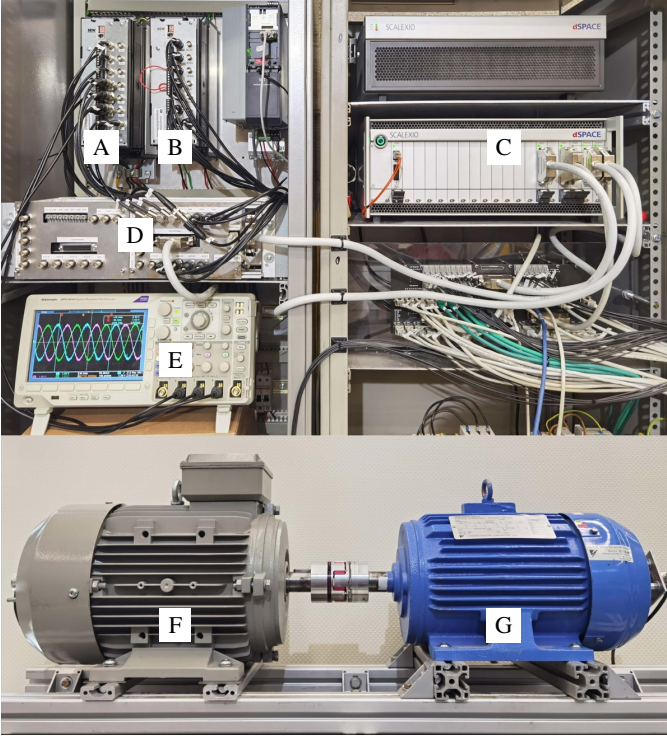
Figure 10. Setup of the electrical drives testbench. A: SEW Inverter for PMSM, B: SEW Inverter for IM, C: dSPACE SCALEXIO real-time control system, D:Interface, E: Oscilloscope, F: IM, G: IPMSM.

Table III
PARAMETERS FOR IM DRIVES

Parameter	Symbol	Value
Rated dc-link voltage	V_{dc}	600 V
Rated power	P_{R}	4 kW
Rated voltage	V_{R}	400 V
Rated current	I_{R}	8.73 A
Rated stator frequency	f_{R}	50 Hz
Rated speed	N_{R}	1430 rpm
Pole pairs	p	2
Stator resistance	R_{s}	2.94 Ω
Rotor resistance	R_{r}	0.67 Ω
Stator leakage inductance	L_{ls}	8.45 mH
Rotor leakage inductance	L_{lr}	8.45 mH
Mutual leakage inductance	L_{m}	195.25 mH

Table IV
PARAMETERS FOR PMSM DRIVES

Parameter	Symbol	Value
Rated dc-link voltage	V_{dc}	600 V
Rated power	P_{R}	3.7 kW
Rated voltage	V_{R}	369 V
Rated current	I_{R}	6.8 A
Rated stator frequency	f_{R}	87.5 Hz
Rated speed	N_{R}	1750 rpm
Pole pairs	p	3
Stator resistance	R_{s}	1.2 Ω
Stator d-axis inductance	L_d	32.93 mH
Stator q-aixs inductance	L_q	37.70 mH
Magnet flux linkage	ψ_{f}	0.67 Wb

doing so, (35)-(39) are repeated to get a new solution $[u_\alpha^1\ u_\beta^1]^\top$ and the corresponding value of the cost function J_1. Note that the optimal solution $\boldsymbol{u}_{\mathrm{opt}}^*$ can only be in the sector where the unconstrained solution $\boldsymbol{u}_{\mathrm{unc}}^*$ locates, e.g., $\overline{AB}$, or in the adjacent sector where the initial guess point P_0 locates, e.g., $\overline{AF}$. Hence, line segments from other adjacent sectors, e.g., $\overline{BC}$, are not considered, as explained in Appendix B.

Based on the above, if

$$J_1 \leq J_A, \qquad (44)$$

point P_1, as shown in Fig. 8, is the optimal solution

$$\boldsymbol{u}_{\mathrm{opt}}^* = \begin{bmatrix} u_\alpha^1 \\ u_\beta^1 \end{bmatrix}. \qquad (45)$$

Otherwise, point A becomes the optimal solution

$$\boldsymbol{u}_{\mathrm{opt}}^* = \begin{bmatrix} u_\alpha^A \\ u_\beta^A \end{bmatrix}. \qquad (46)$$

The complete analytical procedure is illustrated in Fig. 9.

VII. PERFORMANCE EVALUATION

The performance of the proposed methods is examed in the laboratory with two three-phase two-level inverters driving an IM and an IPMSM. The real-time control platform is a dSPACE SCALEXIO system, consisting of a 4GHz Intel XEON processor and a Xilinx Kintex-7 field-programmable gate array (FPGA). Two three-phase two-level SEW MDX inverters are used to control the IM and the IPMSM, respectively. The experimental setup is shown in Fig. 10. The parameters of the IM and the IPMSM drives are given in Tables III and IV, respectively. Finally, the sampling interval T_{s} is 100 µs and the switching frequency is 5 kHz (asymmetric sampling).[6] Note that all results in the following are shown in the per unit (p.u.) system.

A. Experimental Results for the IM Drive System

For an ac motor drive system in the rated condition, i.e. rated dc-link voltage, rated speed and rated current, the unconstrained solution $\boldsymbol{u}_{\mathrm{unc}}^*$ in the steady-state operation is always inside the inverter output voltage limit (hexagon in Fig. 5). More specifically, $\boldsymbol{u}_{\mathrm{unc}}^*$ lies inside the incircle of the hexagon at steady state. Hence, the optimal solution $\boldsymbol{u}_{\mathrm{opt}}^*$ of MPC is equal to $\boldsymbol{u}_{\mathrm{unc}}^*$ in steady state. In this case, the unconstrained MPC with incircle saturation (saturated MPC) $\boldsymbol{u}_{\mathrm{sat}}^*$ is the same as the solution of the constrained MPC in (18).

However, in the transient state, $\boldsymbol{u}_{\mathrm{unc}}^*$ often goes outside the voltage limit. In this case, the saturated MPC directly saturates the output as per (15). The constrained MPC, on the other hand, accounts for the voltage limit to find the optimal switching vector. This implies that, at least in theory, the constrained MPC has the advantage of the optimal full utilization of the dc-link voltage during transient operating conditions. The following experimental results verify the effectiveness of the proposed control methods in transient state.

Fig. 11 shows the experimental results for the IM drive system with three control methods during a current reference

---

[6]For more details on modulation with asymmetric sampling, the reader is referred to [49, Sect. 3.6].
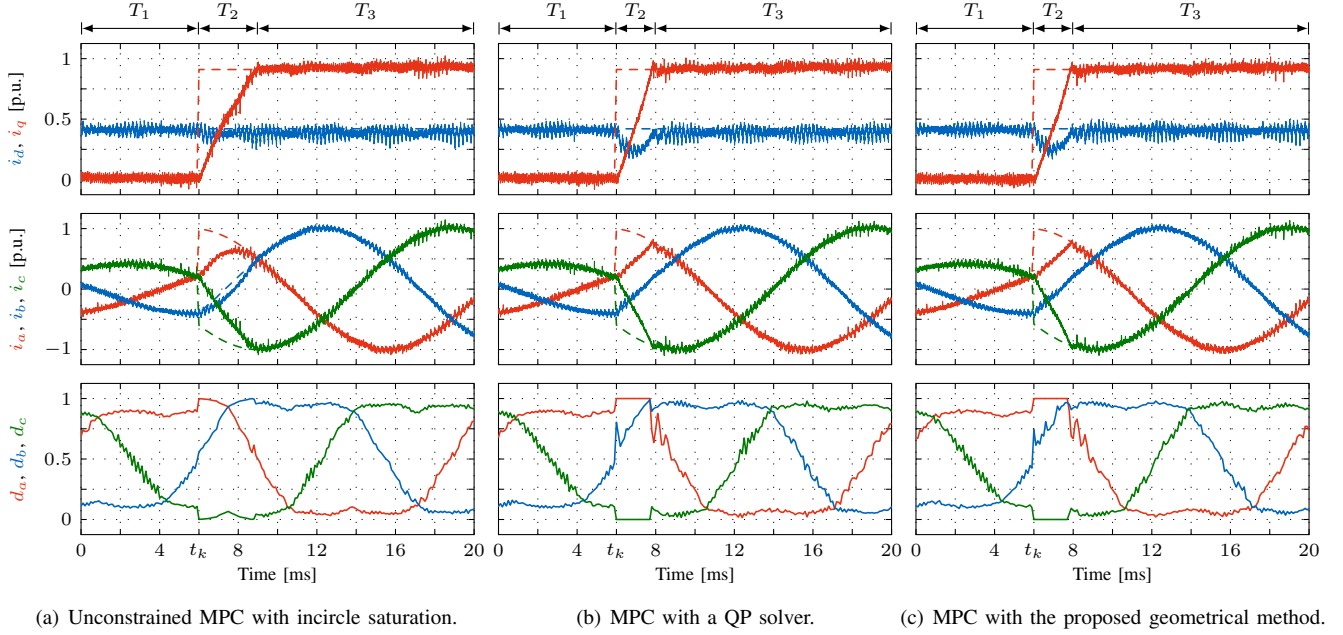
(a) Unconstrained MPC with incircle saturation.   (b) MPC with a QP solver.   (c) MPC with the proposed geometrical method.

Figure 11. Experimental results for the IM drive system. From top to bottom, the waveforms are the d- and q-axis current $\boldsymbol{i}_{dq}$, three-phase current $\boldsymbol{i}_{abc}$ and three-phase duty cycle $\boldsymbol{d}_{abc}$. In the waveforms of $\boldsymbol{i}_{dq}$ and $\boldsymbol{i}_{abc}$, the dashed lines are the reference currents and the solid lines are the measured currents from the oscilloscope with a sampling frequency of 100 kHz.

(a) Unconstrained MPC with incircle saturation.   (b) MPC with a QP solver.   (c) MPC with the proposed geometrical method.
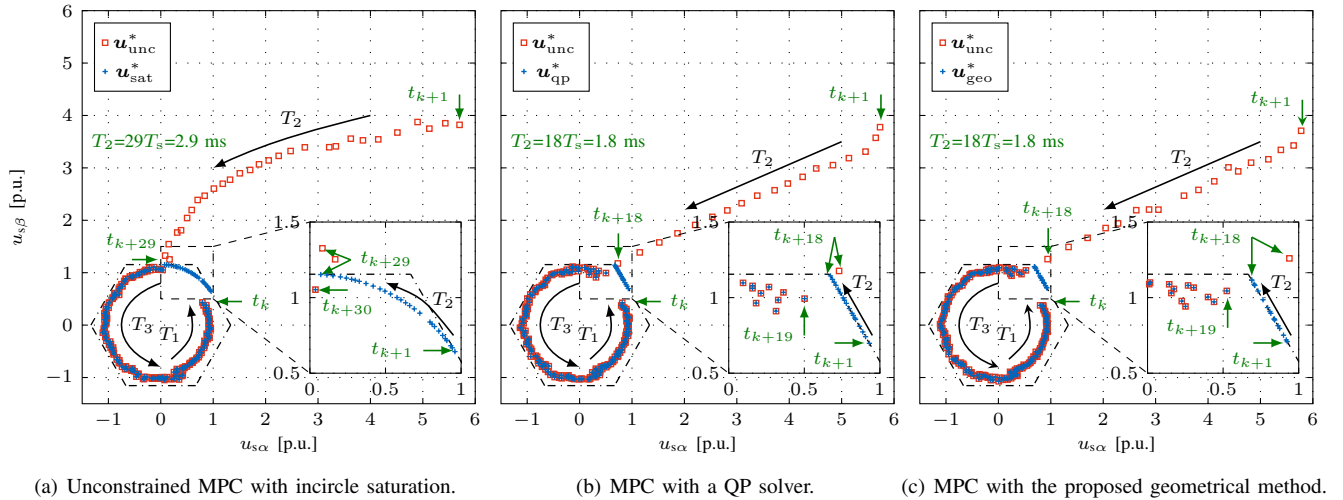
Figure 12. Output voltage of three different methods for the IM drive system

step change, i.e., unconstrained MPC with incircle saturation (left), MPC with a QP solver (middle) and MPC with the proposed geometrical method (right). Note that the adopted QP solver for both the IM and IPMSM drives is the active set method tailored to electrical drives presented in [40]. From top to bottom, the waveforms are the d- and q-axis current $\boldsymbol{i}_{dq}$, three-phase current $\boldsymbol{i}_{abc}$ and three-phase duty cycle $\boldsymbol{d}_{abc}$. The reference of i_q jumps from 0 to 0.91 [p.u.] at time $t_k = 6$ [ms]. As depicted on the top of Fig. 11, the experimental test under discussion can be split into three time intervals, i.e., T_1 (before step), T_2 (during step) and T_3 (after step). T_2 starts at the instant the current reference is stepped up and ends when the measured current reaches the reference value. As expected, and verified in Fig. 11, the behavior of MPC with a QP solver

and MPC with the proposed geometrical method in the interval T_2 is similar, while it is faster than that of the saturated MPC.

For a detailed analysis of the experimental results, it is also necessary to illustrate the output constrained and unconstrained reference voltage in the $\alpha\beta$-plane. In Fig. 12, the points indicated by red square marks ($\square$) are the unconstrained solutions and the points indicated by blue plus marks ($+$) are the constrained solutions. Fig. 12(a) shows the output voltage of saturated MPC in the same time period as shown in Fig. 12(a) (0 - 20 ms). The direction of the arrows (T_1, T_2 and T_3) indicate the trajectory of output voltage changes in time. During the interval T_1, the IM drive operates at steady state meaning that $\boldsymbol{u}_{\text{unc}}^* = \boldsymbol{u}_{\text{sat}}^*$. So $\boldsymbol{u}_{\text{unc}}^*$ ($\square$) and $\boldsymbol{u}_{\text{sat}}^*$ ($+$) coincide. The current reference is stepped up at t_k, forcing

(a) Unconstrained MPC with incircle saturation.

(b) MPC with a QP solver.

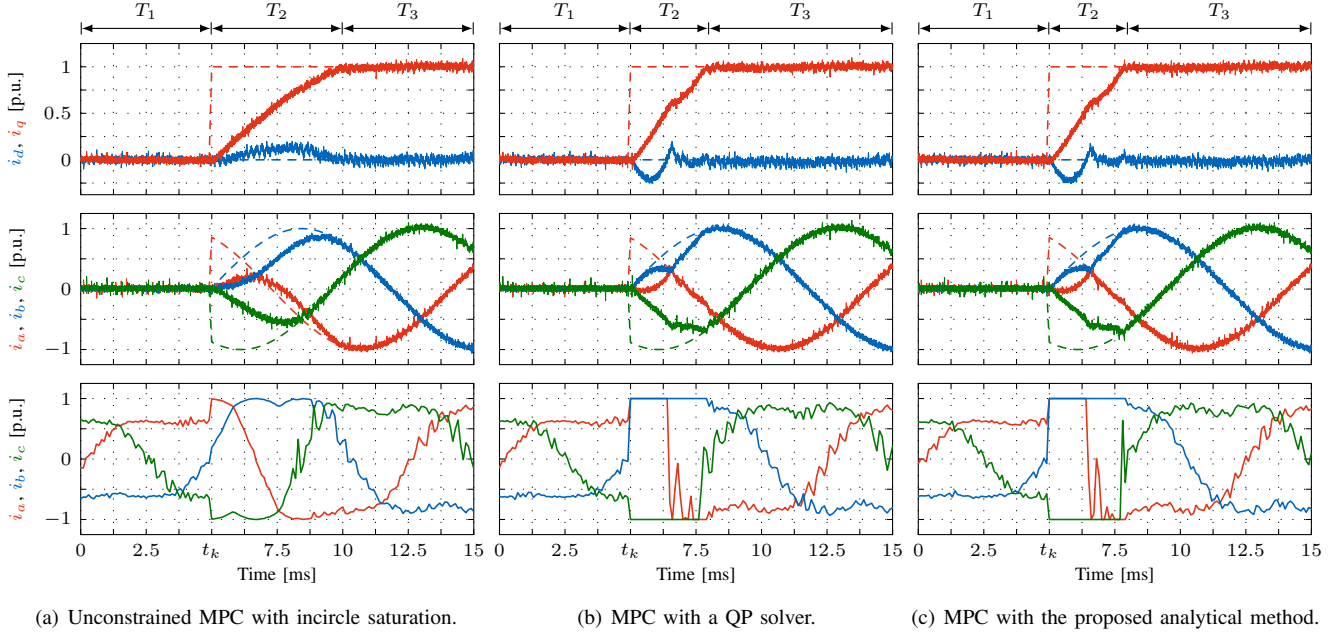(c) MPC with the proposed analytical method.

Figure 13. Experimental results for the IPMSM drive system. From top to bottom, the waveforms are the d- and q-axis current $\boldsymbol{i}_{dq}$, three-phase current $\boldsymbol{i}_{abc}$ and three-phase duty cycle $\boldsymbol{d}_{abc}$. In the waveforms of $\boldsymbol{i}_{dq}$ and $\boldsymbol{i}_{abc}$, the dashed lines are the reference currents and the solid lines are the measured currents from the oscilloscope with a sampling frequency of 100 kHz.
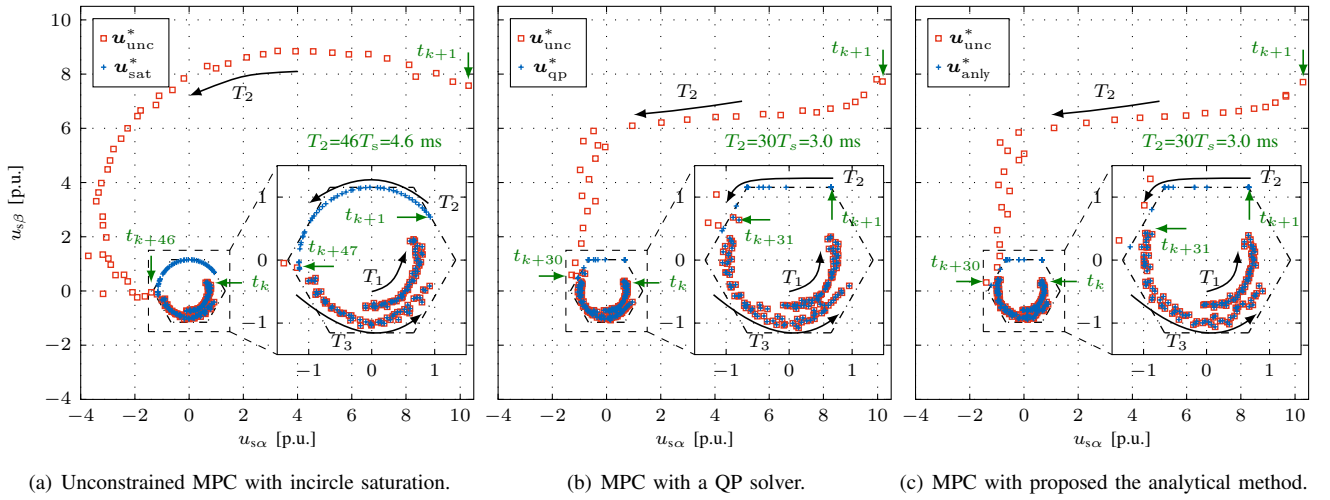

(a) Unconstrained MPC with incircle saturation.

(b) MPC with a QP solver.

(c) MPC with proposed the analytical method.

Figure 14. Output voltage of three different methods for the IPMSM drive system.

$\boldsymbol{u}_{\mathrm{unc}}^*$ to be outside the hexagon at the next time step t_{k+1}. As shown in the zoomed in part of Fig. 12, $\boldsymbol{u}_{\mathrm{sat}}^*$ is limited to the incircle and is different from $\boldsymbol{u}_{\mathrm{unc}}^*$. In the next 29 steps (interval T_2), $\boldsymbol{u}_{\mathrm{sat}}^*$ remains on the border of the incircle and it moves counterclockwise. As the measured current gradually reaches its reference value, $\boldsymbol{u}_{\mathrm{unc}}^*$ also gradually gets closer to $\boldsymbol{u}_{\mathrm{sat}}^*$. From Fig. 12(a) it becomes clear that the interval T_2 lasts 2.9 ms ($29T_{\mathrm{s}}$). From t_{k+30} onwards, the measured current is at its reference value and the drive reaches steady state again. In this period (interval T_3), the $\boldsymbol{u}_{\mathrm{unc}}^*$ and $\boldsymbol{u}_{\mathrm{sat}}^*$ are inside the incircle and overlap again. In Fig. 12(b) and Fig. 12(c), the current reference is also stepped up at t_k. Different from the method in Fig. 12(a), MPC generates the optimal switching vector considering hexagon constraints. In interval T_2, the

solution for MPC with a QP solver $\boldsymbol{u}_{\mathrm{qp}}^*$ and the solution for MPC with the proposed geometrical method $\boldsymbol{u}_{\mathrm{geo}}^*$ stay on the border of the hexagon and move counterclockwise. The MPC with a QP solver and with the proposed method use 40% less time ($T_2 = 18T_{\mathrm{s}} = 1.8$ ms) to reach the new reference value. Fig. 12(b) and Fig. 12(c) also show that MPC with the proposed geometrical method generates almost the same output voltage as with the QP solver.[7]

_____

[7]In theory, these two methods should give the same results and this is validated by simulations. Here the slight difference is due to the experimental environment, e.g., stochastic measurement noise and parameter variation in different tests.

B. Experimental Results for the IPMSM Drive System

As analysed in Section IV, contour map of the IPMSM MPC problem is ellipsoidal, thus rendering the geometrical method unsuitable for such drive systems. To address this, MPC with the proposed analytical solution is applied to the IPMSM system. As with the IM drive system, the dynamic behaviour of the proposed analytical solution for IPMSM drive system is tested by applying a positive current step to the system (i_q from 0 to 1 p.u.) as shown in Fig. 13. Obviously, the proposed analytical method has almost[8] the same performance as the QP solver, and these two MPC methods have much faster transient response than the saturated MPC.

Fig. 14 shows the output voltage of the three different methods for the IPMSM drive system. As before, intervals T_1 and T_3 correspond to the steady-state operation, while the transient takes place during interval T_2. The current reference is stepped up at t_k forcing $\boldsymbol{u}_{\text{unc}}^*$ to be outside the hexagon at the next time step t_{k+1}. $\boldsymbol{u}_{\text{sat}}^*$ is saturated to the incircle in the next 46 steps ($T_2 = 46T_s = 4.6$ ms) as shown in the zoomed in part of Fig. 14(a). In Fig. 14(b) and Fig. 14(c) we can see that optimal solutions of MPC with a QP solver $\boldsymbol{u}_{\text{qp}}^*$ and the proposed analytical method $\boldsymbol{u}_{\text{anly}}^*$ are on the border of the hexagon for the next 30 steps ($T_2 = 30T_s = 3$ ms); the current reaches the reference at t_{k+30} with 34% less time compared with MPC which saturates the unconstrained solution.

C. Steady-State Performance in Overmodulation Region

This paper focuses on the design of fast solving methods for indirect MPC that improves the dynamic performance of ac drives in the presence of output voltage constraints. From the results shown in Figs. 11 to 14 it can be seen that MPC either with a QP solver or with the proposed solving methods enters into the overmodulation (also called non-linear modulation) region only momentarily, i.e., during transients, when full utilization of the dc-link voltage is required. After the transient, the converter operates in the linear modulation region. This process is also referred to as dynamic overmodulation scheme [50].

On the other hand, the steady-state operation of indirect MPC in the overmodulation region is an emerging research topic in the field of electrical drives [51], [52]. Hence, the proposed methods are also examined for drive systems operating in the overmodulation region at steady state. To avoid repetition, only the performance of MPC with the proposed analytical method for IPMSM drives is examined here, see Fig. 15 and 16. The geometrical method for IM drive systems has similar behavior. Usually, the drive system can enter overmodulation range by increasing the speed of the motor. Due to the limitation of the hardware in the used motor test bench, the IPMSM cannot run at a very high speed. Hence, the dc-link voltage is decreased instead of increasing the speed such that operation in the overmodulation region is achieved. In Fig. 15, from left to right, the dc-link voltages $V_{\text{dc}} = 450$V, $V_{\text{dc}} = 420$V and $V_{\text{dc}} = 400$V are applied, respectively, and the speed is controlled at 1200 rpm.

In Fig. 15(a), the IPMSM is operated at the border of the linear modulation region[9] ($m \approx 0.907$). In Fig. 15(b) and in Fig. 15(c), the IPMSM operates in overmodulation region I and overmodulation region II, respectively. Fig. 16 shows the output voltage of the proposed method in the different modulation regions. In Fig. 16(a), the output voltage is on the incircle of the hexagon. In Fig. 16(b), the output voltage mainly moves along the hexagon except when being close to the six vertices, as also indicated by the duty cycle waveforms in Fig. 15(b). In Fig. 16(c), the output voltage is always on the boundaries of the hexagon, as can also be seen from the saturated duty cycle waveforms in Fig. 15(c).

All the results in Fig. 15 and 16 indicate that MPC with the proposed solving methods can successfully operate the IPMSM drive in the overmodulation region although there exists a small offset between the reference and measured current. This can be clearly observed from the q-axis current in Fig. 15(c). This problem can be solved by integrating a harmonic reference generator (HRG) into the proposed MPC methods. Readers can refer to [51], [52] for the design of HRG for indirect MPC. Moreover, with the HRG, the working region of the indirect MPC can be extended to six-step operation.

D. Comparison of the Dynamic Performance

To enable a visual comparison, the current responses on the q-axis of all the methods for IM and IPMSM drive systems are presented in Fig. 17. $i_{q,\text{anly}}$ and $i_{q,\text{qp}}$ (see the red line) are the current responses of MPC with the analytical method and MPC with a QP solver, respectively. The blue line ($i_{q,\text{geo}}$) is the current response of MPC with the geometrical method, and the green line ($i_{q,\text{sat}}$) is the current response of saturated MPC.

As can be observed in Fig. 17(a), $i_{q,\text{anly}}$, $i_{q,\text{qp}}$ and $i_{q,\text{geo}}$ have the same dynamic performance, which means that the analytical method can also be applied to isotropic machines, e.g., IMs and SPMSMs. However, as shown in Fig. 9, the geometrical method is much simpler than the analytical methods, hence, it is still recommended to use it with isotropic machines.

In Fig. 17(b), $i_{q,\text{anly}}$ and $i_{q,\text{qp}}$ overlap as expected (see the current shown in red). The green line is the current response of saturated MPC, which, as expected, is the slowest method. Moreover, to provide more insight, the geometrical method is also employed for the IPMSM MPC problem. Although the geometrical method is originally designed for isotropic machines, e.g., IMs and SPMSMs, it still manages to find a sufficiently good suboptimal solution for anisotropic machines, such as IPMSMs, so long as the saliency ratio (L_q/L_d) of the machine is close to 1. In the examined case, the saliency ratio of the IPMSM is 1.14, so the $i_{q,\text{geo}}$ reaches the reference current a little slower than $i_{q,\text{anly}}$. The difference between $i_{q,\text{geo}}$ and $i_{q,\text{anly}}$ becomes bigger with an increasing saliency ratio.

---

[8]Here the slight difference is also due to the experimental environment.

[9]The modulation index m and the overmodulation region are defined in this paper according to [53].

(a) Linear modulation region: $m \in [0, 0.907)$. (b) Overmodulation region I: $m \in [0.907, 0.957)$ (c) Overmodulation region II: $m \in [0.957, 1)$.
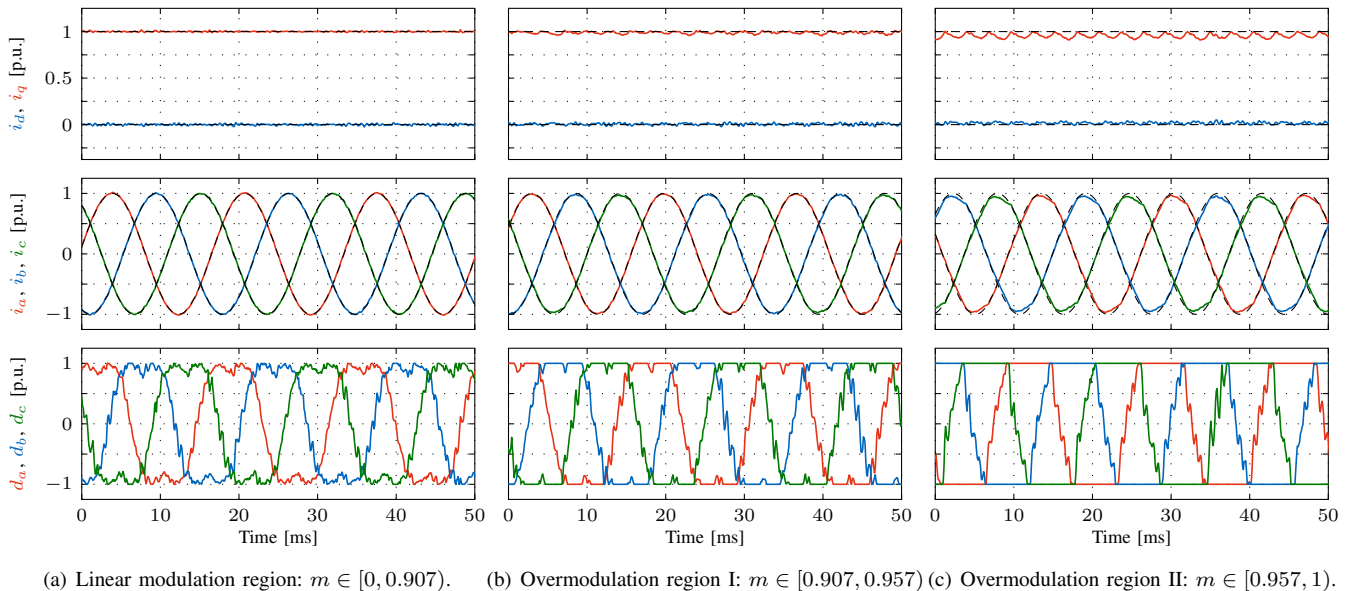
Figure 15. Experimental results for the IPMSM drive system operating in the overmodulation region. From top to bottom, the waveforms are the d- and q-axis current $\boldsymbol{i}_{dq}$, three-phase current $\boldsymbol{i}_{abc}$ and three-phase duty cycle $\boldsymbol{d}_{abc}$. In the waveforms of $\boldsymbol{i}_{dq}$ and $\boldsymbol{i}_{abc}$, the dashed lines are the reference currents and the solid lines are the measured currents from dSPACE with a sampling frequency of 10 kHz. From left to right, the dc-link voltages $V_{\mathrm{dc}} = 450\mathrm{V}$, $V_{\mathrm{dc}} = 420\mathrm{V}$ and $V_{\mathrm{dc}} = 400\mathrm{V}$ are applied, respectively.

(a) Linear modulation region: $m \in [0, 0.907)$. (b) Overmodulation region I: $m \in [0.907, 0.957)$ (c) Overmodulation region II: $m \in [0.957, 1)$.
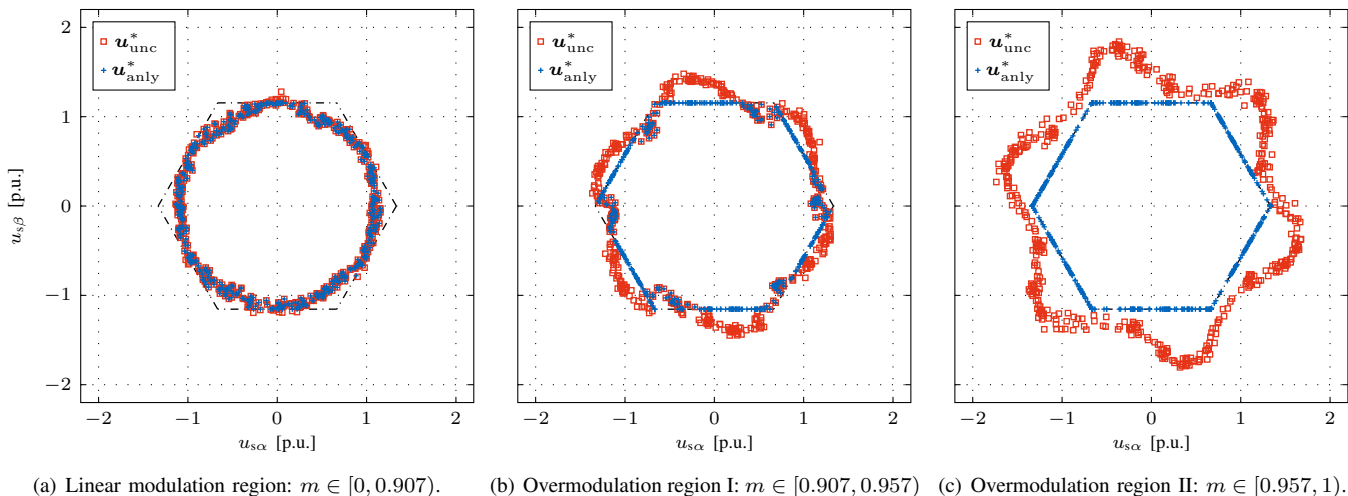
Figure 16. Output voltage of the proposed method for the IPMSM drive system operating in the overmodulation region.

E. Computational Burden

Since the computational burden is a key factor in the evaluation of the solution for indirect MPC, the maximum (i.e., worst-case scenario) turnaround times $t_{\max}$ of the four discussed control algorithms applied to IPMSM drives are summarized in Table V. Moreover, to better highlight the benefits of the proposed solving methods and allow for more meaningful conclusions, the two recently proposed fast solvers from [41], [42] are also implemented on the same control platform and their corresponding turnaround times are also reported in Table V. It is worth mentioning that, the time in Table V is only the computation time required for finding the (sub)optimal solution with a given method and it does not relate to the computation time of the whole control scheme. As can be seen, unconstrained MPC with incircle saturation

and the proposed geometrical method demonstrate similar computation times (0.7 μs and 0.8 μs). Note, however, that the geometrical method shows much better dynamic performance than the saturated MPC according to the results in Fig 17. The computation time of MPC with the analytical method is 1.8 μs, which is still very small compared to that required with the QP solver (3.7 μs). Note that the QP solver used here is a tailored solver for electrical drives based on the algorithm in [40]. Common off-the-shelf QP solvers for generic QPs typically need much more computation time. For example, the solvers developed in [41] and [42]—which are used here for benchmarking purposes—are faster than off-the-shelf solvers, such as the qpOASES [37], by a factor of four. Considering the turnaround times reported in Table V, it can be deduced that the proposed analytical and geometrical solving methods
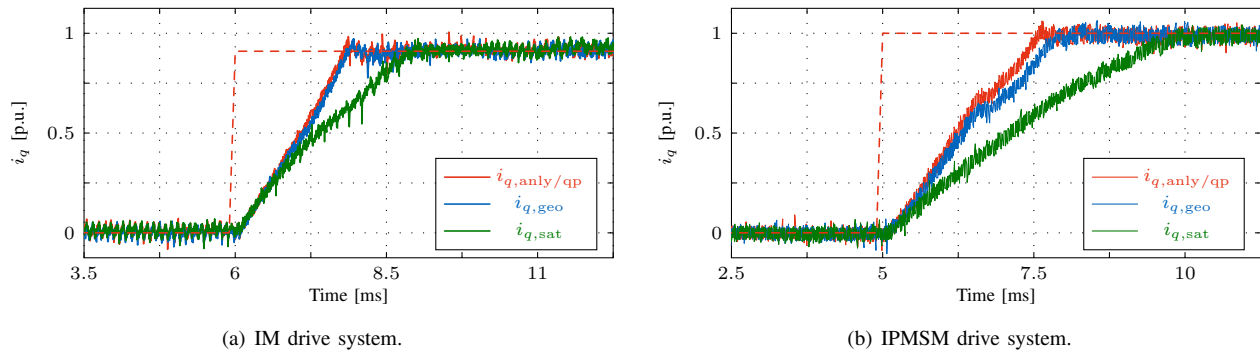
(a) IM drive system.

(b) IPMSM drive system.

Figure 17. Comparison of the dynamic performance of different methods for IM and IPMSM drive systems.

Table V
THE MAXIMUM TURNAROUND TIME t_{max} OF THE DISCUSSED CONTROL ALGORITHMS RUNNING ON DSPACE.

Method	Saturated MPC	Geometrical Method	Analytical Method	Fast Solver [41]	aVsIs [42]	QP Solver
Turnaround time t_{max} (µs)	0.7	0.8	1.8	2.3	2.8	3.7
Proportion relative to QP	19%	22%	49%	62%	76%	100%

clearly outperform such solvers.

The proportion of the computation times relative to that of the QP solver are also listed in Table V. Although the computation times differ when these methods are implemented on different control platforms, the relative time remains the similar to the one presented here. Hence, these proportions in Table V indicate that both proposed methods can dramatically reduce the computational burden while achieving favourable dynamic performance, making them suitable for industrial applications.

VIII. CONCLUSION

This paper presented two simple methods to solve the optimization problem of indirect MPC for electrical drives in a computationally efficient manner. By analysing the contour maps of the indirect MPC optimization problem for IM and IPMSM drive systems, the optimal solution can be found by adopting a suitable computational method. More specifically, a geometrical method is proposed for IM drives and an analytical method is proposed for IPMSM drives. Both proposed algorithms are experimentally tested and compared with MPC solved with tailored efficient QP solvers. The comparison shows that the proposed methods have the same steady-state and dynamic performance as MPC with QP solvers while significantly reducing the computational burden. Based on the presented analysis and result, it can be claimed that the proposed solutions can be easily implemented on industrial control platforms while still exploiting the superior performance MPC typically achieves.

APPENDIX A
COEFFICIENTS FOR GEOMETRICAL METHOD

The coefficients of the quadratic function in (37) are

$$a_q = (m_{11} + m_{12}a)^2 + (m_{21} + m_{22}a)^2 + \lambda(1 + a^2),$$
$$b_q = 2((m_{11} + m_{12}a)(m_{12}b + r_1)$$
$$\quad + (m_{21} + m_{22}a)(m_{22}b + r_2) + \lambda(ab - u_{\alpha 0} - a u_{\beta 0})),$$
$$c_q = (m_{12}b + r_1)^2 + (m_{22}b + r_2)^2$$
$$\quad + \lambda(u_{\alpha 0}^2 + (b - a u_{\beta 0})^2).$$

APPENDIX B
DETERMINATION OF VOLTAGE CONSTRAINTS

The analysis about which voltage constraints should be considered in the analytical method is provided here. To this aim, consider the case shown in Fig. 8 as example. In this case, the unconstrained solution G locates in sector 1 and the initial guess point P_0 is in sector 6.

As shown in Fig. 18, sector 1 can be divided into 2 areas, i.e., I and II. According to the analysis in Section IV, the contour map of the indirect MPC problem for anisotropic machine drives is elliptical. For the elliptical contour, when G locates in area I, it is clear that the cost function at point A is smaller than any other point on the line segment $\overline{AB}$, e.g., $J_A < J_B$. Moreover, for line segment $\overline{BC}$, the gradient descent direction is from C to B. In this case, J_B is the smallest along $\overline{BC}$. This means J_A is smaller than at any point on $\overline{BC}$. Hence, the constraints $\overline{BC}$ should not be considered in the calculation of the optimal solution when P_0 is in sector 6.

Similarly, when G is in area II, J_A is still the smaller than at any other point on $\overline{BC}$. Nevertheless, it is possible that the value of the cost function varies in a non-monotonic way along $\overline{AF}$ implying that it exists a point P_1 on $\overline{AF}$ with $J_{P_1} < J_A$. In this case, $\overline{AF}$ needs to be checked.
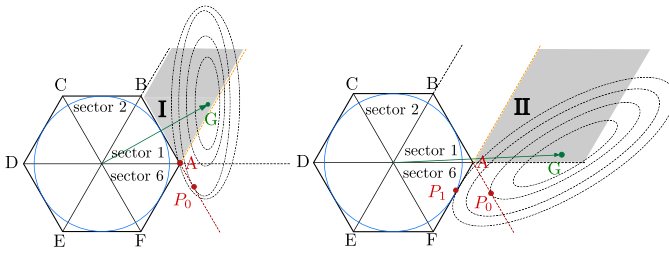
Figure 18. Voltage constraints considered for analytical method.

Based on the above analysis it can be concluded that the optimal solution is either in the sector where the unconstrained solution locates, or in the sector adjacent to where the initial guess point P_0 is.

REFERENCES

[1] P. Cortes, M. Kazmierkowski, R. Kennel, D. Quevedo, and J. Rodriguez, "Predictive control in power electronics and drives," *IEEE Transactions on Industrial Electronics*, vol. 55, no. 12, pp. 4312–4324, dec 2008.

[2] S. Kouro, P. Cortes, R. Vargas, U. Ammann, and J. Rodriguez, "Model predictive control—a simple and powerful method to control power converters," *IEEE Transactions on Industrial Electronics*, vol. 56, no. 6, pp. 1826–1838, jun 2009.

[3] S. Vazquez, J. Rodriguez, M. Rivera, L. G. Franquelo, and M. Norambuena, "Model predictive control for power converters and drives: Advances and trends," *IEEE Transactions on Industrial Electronics*, vol. 64, no. 2, pp. 935–947, feb 2017.

[4] P. Karamanakos, E. Liegmann, T. Geyer, and R. Kennel, "Model predictive control of power electronic systems: Methods, results, and challenges," *IEEE Open Journal of Industry Applications*, vol. 1, pp. 95–114, 2020.

[5] P. Stolze, M. Tomlinson, R. Kennel, and T. Mouton, "Heuristic finite-set model predictive current control for induction machines," in *2013 IEEE ECCE Asia Downunder*, 2013, pp. 1221–1226.

[6] F. Wang, S. Li, X. Mei, W. Xie, J. Rodriguez, and R. M. Kennel, "Model-based predictive direct control strategies for electrical drives: An experimental evaluation of PTC and PCC methods," *IEEE Transactions on Industrial Informatics*, vol. 11, no. 3, pp. 671–681, jun 2015.

[7] W. Xie, X. Wang, F. Wang, W. Xu, R. M. Kennel, D. Gerling, and R. D. Lorenz, "Finite-control-set model predictive torque control with a deadbeat solution for PMSM drives," *IEEE Transactions on Industrial Electronics*, vol. 62, no. 9, pp. 5402–5410, sep 2015.

[8] X. Liu, J. Wang, X. Gao, W. Tian, L. Zhou, and R. Kennel, "Robust predictive speed control of SPMSM drives with algebraically designed weighting factors," *IEEE Transactions on Power Electronics*, vol. 37, no. 12, pp. 14434–14446, dec 2022.

[9] J. Rodriguez, M. P. Kazmierkowski, J. R. Espinoza, P. Zanchetta, H. Abu-Rub, H. A. Young, and C. A. Rojas, "State of the art of finite control set model predictive control in power electronics," *IEEE Transactions on Industrial Informatics*, vol. 9, no. 2, pp. 1003–1016, may 2013.

[10] T. Geyer, G. Papafotiou, and M. Morari, "Model predictive direct torque control—part i: Concept, algorithm, and analysis," *IEEE Transactions on Industrial Electronics*, vol. 56, no. 6, pp. 1894–1905, jun 2009.

[11] T. Geyer, N. Oikonomou, G. Papafotiou, and F. D. Kieferndorf, "Model predictive pulse pattern control," *IEEE Transactions on Industry Applications*, vol. 48, no. 2, pp. 663–676, mar 2012.

[12] Q. Yang, P. Karamanakos, W. Tian, X. Gao, X. Li, T. Geyer, and R. Kennel, "Computationally efficient fixed switching frequency direct model predictive control," *IEEE Transactions on Power Electronics*, vol. 37, no. 3, pp. 2761–2777, mar 2022.

[13] Y. Wu, Z. Zhang, Q. Yang, W. Tian, P. Karamanakos, M. L. Heldwein, and R. Kennel, "A direct model predictive control strategy with an implicit modulator for six-phase PMSMs," *IEEE Journal of Emerging and Selected Topics in Power Electronics*, pp. 1–1, 2022.

[14] Z. Zhang, C. M. Hackl, and R. Kennel, "Computationally efficient DMPC for three-level NPC back-to-back converters in wind turbine systems with PMSG," *IEEE Transactions on Power Electronics*, vol. 32, no. 10, pp. 8018–8034, oct 2017.

[15] T. Geyer and D. E. Quevedo, "Multistep finite control set model predictive control for power electronics," *IEEE Transactions on Power Electronics*, vol. 29, no. 12, pp. 6836–6846, dec 2014.

[16] T. Geyer, *Model predictive control of high power converters and industrial drives*. Chichester, West Sussex, UK: John Wiley & Sons, Inc, 2016.

[17] P. Karamanakos, T. Geyer, and R. P. Aguilera, "Computationally efficient long-horizon direct model predictive control for transient operation," in *2017 IEEE Energy Conversion Congress and Exposition (ECCE)*. IEEE, oct 2017.

[18] ——, "Long-horizon direct model predictive control: Modified sphere decoding for transient operation," *IEEE Transactions on Industry Applications*, vol. 54, no. 6, pp. 6060–6070, nov 2018.

[19] P. Acuna, C. A. Rojas, R. Baidya, R. P. Aguilera, and J. E. Fletcher, "On the impact of transients on multistep model predictive control for medium-voltage drives," *IEEE Transactions on Power Electronics*, vol. 34, no. 9, pp. 8342–8355, sep 2019.

[20] S. Kouro, M. A. Perez, J. Rodriguez, A. M. Llor, and H. A. Young, "Model predictive control: MPC's role in the evolution of power electronics," *IEEE Industrial Electronics Magazine*, vol. 9, no. 4, pp. 8–21, dec 2015.

[21] J. Rodriguez, C. Garcia, A. Mora, F. Flores-Bahamonde, P. Acuna, M. Novak, Y. Zhang, L. Tarisciotti, S. A. Davari, Z. Zhang, F. Wang, M. Norambuena, T. Dragicevic, F. Blaabjerg, T. Geyer, R. Kennel, D. A. Khaburi, M. Abdelrahem, Z. Zhang, N. Mijatovic, and R. P. Aguilera, "Latest advances of model predictive control in electrical drives—part i: Basic concepts and advanced strategies," *IEEE Transactions on Power Electronics*, vol. 37, no. 4, pp. 3927–3942, apr 2022.

[22] P. Karamanakos, R. Mattila, and T. Geyer, "Fixed switching frequency direct model predictive control based on output current gradients," in *IECON 2018 - 44th Annual Conference of the IEEE Industrial Electronics Society*. IEEE, oct 2018.

[23] A. A. Ahmed, B. K. Koh, and Y. I. Lee, "A comparison of finite control set and continuous control set model predictive control schemes for speed control of induction motors," *IEEE Transactions on Industrial Informatics*, vol. 14, no. 4, pp. 1334–1346, apr 2018.

[24] F. Wang, L. He, and J. Rodriguez, "FPGA-based continuous control set model predictive current control for PMSM system using multistep error tracking technique," *IEEE Transactions on Power Electronics*, vol. 35, no. 12, pp. 13455–13464, dec 2020.

[25] A. Zanelli, J. Kullick, H. M. Eldeeb, G. Frison, C. M. Hackl, and M. Diehl, "Continuous control set nonlinear model predictive control of reluctance synchronous machines," *IEEE Transactions on Control Systems Technology*, vol. 30, no. 1, pp. 130–141, jan 2022.

[26] K. Bandy and P. Stumpf, "Quadratic regression model-based indirect model predictive control of AC drives," *IEEE Transactions on Power Electronics*, vol. 37, no. 11, pp. 13158–13177, nov 2022.

[27] A. Linder and R. Kennel, "Model predictive control for electrical drives," in *IEEE 36th Conference on Power Electronics Specialists, 2005*. IEEE, 2005.

[28] S. Mariethoz, A. Domahidi, and M. Morari, "Sensorless explicit model predictive control of permanent magnet synchronous motors," in *2009 IEEE International Electric Machines and Drives Conference*. IEEE, may 2009.

[29] S. Bolognani, S. Bolognani, L. Peretti, and M. Zigliotto, "Design and implementation of model predictive control for electrical motor drives," *IEEE Transactions on Industrial Electronics*, vol. 56, no. 6, pp. 1925–1936, jun 2009.

[30] F. Toso, P. G. Carlet, A. Favato, and S. Bolognani, "On-line continuous control set MPC for PMSM drives current loops at high sampling rate using qpOASES," in *2019 IEEE Energy Conversion Congress and Exposition (ECCE)*. IEEE, sep 2019.

[31] G. Cimini, D. Bernardini, S. Levijoki, and A. Bemporad, "Embedded model predictive control with certified real-time optimization for synchronous motors," *IEEE Transactions on Control Systems Technology*, vol. 29, no. 2, pp. 893–900, mar 2021.

[32] X. Jiang, Y. Yang, M. Fan, A. Ji, Y. Xiao, X. Zhang, W. Zhang, C. Garcia, S. Vazquez, and J. Rodriguez, "An improved implicit model predictive current control with continuous control set for PMSM drives," *IEEE Transactions on Transportation Electrification*, vol. 8, no. 2, pp. 2444–2455, jun 2022.

[33] P. G. Carlet, A. Favato, S. Bolognani, and F. Dorfler, "Data-driven continuous-set predictive current control for synchronous motor drives," *IEEE Transactions on Power Electronics*, vol. 37, no. 6, pp. 6637–6646, jun 2022.

[34] E. Camacho and C. Bordons, *Model Predictive Control*, 2nd ed. Springer, 2013.

[35] J. Nocedal and S. Wright, *Numerical Optimization*, 2nd ed. Springer, 2006.

[36] D. Kouzoupis, A. Zanelli, H. Peyrl, and H. J. Ferreau, "Towards proper assessment of QP algorithms for embedded model predictive control," in *2015 European Control Conference (ECC)*. IEEE, jul 2015.

[37] H. J. Ferreau, C. Kirches, A. Potschka, H. G. Bock, and M. Diehl, "qpOASES: a parametric active-set algorithm for quadratic programming," *Mathematical Programming Computation*, vol. 6, no. 4, pp. 327–363, apr 2014.

[38] S. Hanke, O. Wallscheid, and J. Bocker, "Continuous-control-set model predictive control with integrated modulator in permanent magnet synchronous motor applications," in *2019 IEEE International Conference on Electric Machines and Drives (IEMDC)*. IEEE, may 2019.

[39] M. Rossi, P. Karamanakos, and F. Castelli-Dezza, "An indirect model predictive control method for grid-connected three-level neutral point clamped converters with LCL filters," *IEEE Transactions on Industry Applications*, vol. 58, no. 3, pp. 3750–3768, may 2022.

[40] Q. Duan, W. Tian, Q. Yang, X. Gao, Y. Mao, P. Karamanakos, R. Kennel, and M. L. Heldwein, "Computationally efficient overmodulation methods for synchronous motor drive systems," *IEEE Transactions on Industrial Informatics*, pp. 1–13, 2022.

[41] A. Favato, P. G. Carlet, F. Toso, R. Torchio, L. Ortombina, M. Bruschetta, R. Carli, P. Alotto, S. Bolognani, and J. Rodriguez, "Fast solver for implicit continuous set model predictive control of electric drives," *IEEE Access*, vol. 10, pp. 17 430–17 440, 2022.

[42] I. D. D. Martin, D. Pasqualotto, and F. Tinazzi, "aVsIs: An analytical-solution-based solver for model-predictive control with hexagonal constraints in voltage-source inverter applications," *IEEE Transactions on Power Electronics*, vol. 37, no. 12, pp. 14 375–14 383, dec 2022.

[43] J. Holtz, "The representation of ac machine dynamics by complex signal flow graphs," *IEEE Transactions on Industrial Electronics*, vol. 42, no. 3, pp. 263–271, June 1995.

[44] J. Zou, W. Xu, and C. Ye, "Improved deadbeat control strategy for linear induction machine," *IEEE Transactions on Magnetics*, vol. 53, no. 6, pp. 1–4, jun 2017.

[45] X. Cai, Z. Zhang, J. Wang, and R. Kennel, "Optimal control solutions for PMSM drives: A comparison study with experimental assessments," *IEEE Journal of Emerging and Selected Topics in Power Electronics*, vol. 6, no. 1, pp. 352–362, mar 2018.

[46] S. Richter, T. Geyer, and M. Morari, "Resource-efficient gradient methods for model predictive pulse pattern control on an FPGA," *IEEE Transactions on Control Systems Technology*, vol. 25, no. 3, pp. 828–841, may 2017.

[47] W. Tian, Q. Yang, X. Li, X. Gao, X. Chen, and R. Kennel, "Deadbeat control for AC drive systems with optimal dynamic performance," in *2020 IEEE Energy Conversion Congress and Exposition (ECCE)*. IEEE, oct 2020.

[48] R. Ottersten and J. Svensson, "Vector current controlled voltage source converter-deadbeat control and saturation strategies," *IEEE Transactions on Power Electronics*, vol. 17, no. 2, pp. 279–285, mar 2002.

[49] D. Holmes and T. Lipo, *Pulse Width Modulation for Power Converters: Principles and Practice*, ser. IEEE Press Series on Power and Energy Systems. Wiley, 2003.

[50] J. Yoo and S.-K. Sul, "Dynamic overmodulation scheme for improved current regulation in PMSM drives," *IEEE Transactions on Power Electronics*, vol. 37, no. 6, pp. 7132–7144, jun 2022.

[51] A. Brosch, O. Wallscheid, and J. Bocker, "Model predictive control of permanent magnet synchronous motors in the overmodulation region including six-step operation," *IEEE Open Journal of Industry Applications*, vol. 2, pp. 47–63, 2021.

[52] ——, "Model predictive torque control for permanent- magnet synchronous motors using a stator- fixed harmonic flux reference generator in the entire modulation range," *IEEE Transactions on Power Electronics*, vol. 38, no. 4, pp. 4391–4404, apr 2023.

[53] A. Hava, R. Kerkman, and T. Lipo, "Carrier-based PWM-VSI overmodulation strategies: analysis, comparison, and design," *IEEE Transactions on Power Electronics*, vol. 13, no. 4, pp. 674–689, jul 1998.
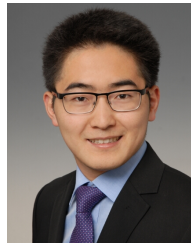
Wei Tian (Member, IEEE) received the B.Eng. degree in electrical engineering and automation from Central South University, Changsha, China, in 2012, and the M.Sc. degree in electrical power engineering from RWTH Aachen University, Aachen, Germany, in 2015. He is currently working towards the Ph.D. degree in electrical engineering with the Chair of Electrical Drive Systems and Power Electronics, and the Chair of High-Power Converter Systems, Technical University of Munich, Munich, Germany.

His research interests include power electronics and electrical drives, model predictive control, and modular multilevel converter.

Qifan Yang (Member, IEEE) was born in Anhui, China, in 1995. He received the B.Eng. degree in electrical engineering Xi'an Jiaotong University, Xi'an, Shannxi, China, in 2016, and the M.Sc. degree in electrical power engineering from Technical University of Munich, Munich, Germany, in 2019.

Since 2019, he has been pursuing the Ph.D. degree in electrical engineering at the Chair of Electrical Drive Systems and Power Electronics, Technical University of Munich (TUM), Germany. His research interests include optimal control, power electronics and electrical drives.

Xiaonan Gao (Member, IEEE) received the B.S. and M.S. degrees from the Dalian University of Technology, Dalian, China, in 2013 and 2016, respectively, and the Dr.-Ing. degree from the Technical University of Munich, Munich, Germany, in 2022, all in electrical engineering.

He is currently a Postdoctoral Fellow with KTH Royal Institute of Technology, Stockholm, Sweden. His research interests include permanent magnet synchronous motor drives, predictive control, and multilevel converters.
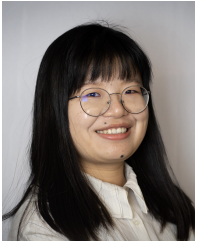
Petros Karamanakos (Senior Member, IEEE) received the Diploma and Ph.D. degrees in electrical and computer engineering from the National Technical University of Athens (NTUA), Athens, Greece, in 2007, and 2013, respectively.

From 2010 to 2011 he was with the ABB Corporate Research Center, Baden-Dättwil, Switzerland, where he worked on model predictive control strategies for medium-voltage drives. From 2013 to 2016 he was a PostDoc Research Associate in the Chair of Electrical Drive Systems and Power Electronics, Technische Universität München, Munich, Germany. Since 2016, he has been with the Faculty of Information Technology and Communication Sciences, Tampere University, Tampere, Finland, where he is currently an Associate Professor. His main research interests lie at the intersection of optimal control, mathematical programming and power electronics, including model predictive control and optimal modulation for utility-scale power converters and ac variable speed drives.

Dr. Karamanakos received the 2014 Third Best Paper Award of the IEEE Transactions on Industry Applications and three Prize Paper Awards at conferences. He serves as an Associate Editor of the IEEE Transactions on Industry Applications and of the IEEE Open Journal of Industry Applications. He is a Regional Distinguished Lecturer of the IEEE Power Electronics Society in the years 2022 and 2023.

Xingqi Yin received the B.Eng. degree in electrical engineering and automation from China University of Petroleum (East China), Qingdao, China, in 2019 and the M.Sc. Degree in electrical and computer engineering from Technical University of Munich (TUM), Munich, Germany, in 2022, where she is currently working toward the Ph.D. degree in electrical engineering at the Chair of High-Power Converter Systems.

Her research interests include power electronics, active filters and electromagnetic compatibility.

Ralph Kennel (Life Senior Member, IEEE) was born in Kaiserslautern, Germany, in 1955. He received the Diploma and Dr. Ing. (Ph.D.) degrees in electrical engineering from the University of Kaiserslautern, Kaiserslautern, Germany, in 1979 and 1984, respectively.

From 1983 to 1999, he worked on several positions with Robert BOSCH GmbH (Germany). Until 1997, he was responsible for the development of servo drives. From 1994 to 1999, he was a Visiting Professor with the University of Newcastle upon Tyne, Newcastle upon Tyne, U.K. From 1999 to 2008, he was a Professor of electrical machines and drives with Wuppertal University, Wuppertal, Germany. Since 2008, he has been a Professor of electrical drive systems and power electronics with Technical University of Munich, Munich, Germany. His current main interests include renewable energy systems, sensorless control of ac drives, predictive control of power electronics, and hardware-in-the-loop systems.

Dr. Kennel is a Fellow of the IEE and a Chartered Engineer in the U.K. Within IEEE, he is a Treasurer of the Germany Section as well as ECCE Global Partnership Chair of the Power Electronics society. He is an Associate Editor for the IEEE Transactions on Power Electronics.

Marcelo Lobo Heldwein (Senior Member, IEEE) received the B.S. and M.S. degrees in electrical engineering from the Federal University of Santa Catarina (UFSC), Florianópolis, Brazil, in 1997 and 1999, respectively, and his Ph.D. degree in electrical engineering from the Swiss Federal Institute of Technology (ETH Zurich), Zurich, Switzerland, in 2007.

From 1999 to 2003, he worked with industry, including R&D activities at the Power Electronics Institute, Brazil and Emerson Network Power, in Brazil and Sweden. He was a Postdoctoral Fellow at the ETH Zurich and at the UFSC from 2007 to 2009. From 2010 to 2022 he was a Professor with the Department of Electronics and Electrical Engineering at the UFSC. He is currently the head of the Chair of High-Power Converter Systems with TUM School of Engineering and Design at the Technical University of Munich (TUM), Munich, Germany. His research interests include Power Electronics, Advanced Power Distribution Technologies and Electromagnetic Compatibility.

Dr. Heldwein is a member of the Brazilian Power Electronic Society (SOBRAEP) and a member of the Advisory Board of PCIM Europe.